Science of the Total Environment 897 (2023) 165367

Contents lists available at ScienceDirect

Science of the Total Environment

journal homepage: www.elsevier.com/locate/scitotenv

Regulation of deep carbon degassing by gas-rock-water interactions in a seismic region of Southern Italy

Dario Buttitta [a,b,*], Giorgio Capasso [a], Michele Paternoster [a,b], Marino Domenico Barberio [c], Francesca Gori [d], Marco Petitta [d], Matteo Picozzi [e], Antonio Caracausi [a,f,*]

[a] Istituto Nazionale di Geofisica e Vulcanologia, Sezione di Palermo, Palermo, 90146, Italy
[b] University of Basilicata, Department of Sciences, Potenza, 85100, Italy
[c] Istituto Nazionale di Geofisica e Vulcanologia, Sezione di Roma 1, Roma, 00143, Italy
[d] Sapienza University of Rome, Department of Earth Sciences, Rome, 00185, Italy
[e] University of Naples Federico II, Department of Physics 'Ettore Pancini', Naples, 80126, Italy
[f] Universidad de Salamanca, Departamento de Geología, Salamanca, 37008, Spain

HIGHLIGHTS

- Deep CO_2 (free/dissolved) comes from a source with $\delta^{13}C_{CO_2}$ of 2.3 ‰ to +3.20 ‰.
- Our model estimate CO_2 output in atmosphere at least 40 % higher than others approach.
- CO_2 high emissions from study area overlap with several global volcanic sites.
- Difficulty in attributing origin of CO_2 source due to gas-rock equilibrium

GRAPHICAL ABSTRACT

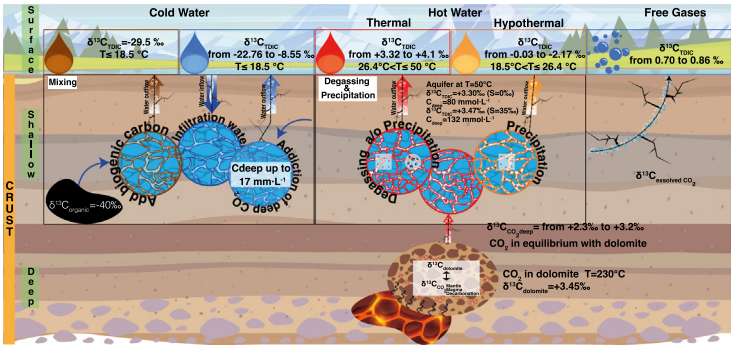

ARTICLE INFO

Editor: Christian Herrera

Keywords:
Noble gases
Carbon isotopes
CO_2 output
Degassing
Precipitation
Earthquakes

ABSTRACT

This study is focused on fluids characterization and circulations through the crust of the Irpinia region, an active seismic zone in Southern Italy, that has experienced several high-magnitude earthquakes, including a catastrophic one in 1980 (M = 6.9 Ms). Using isotopic geochemistry and the carbon-helium system in free and dissolved volatiles in water, this study aims to explore the processes at depth that can alter pristine chemistry of these natural fluids. Gas-rock-water interactions and their impact on CO_2 emissions and isotopic composition are evaluated using a multidisciplinary model that integrates geochemistry and regional geological data. By analyzing the He isotopic signature in the natural fluids, the release of mantle-derived He on a regional scale in Southern Italy is verified, along with significant emissions of deep-sourced CO_2. The proposed model, supported by geological and geophysical constraints, is based on the interactions between gas, rock, and water within the crust and the degassing of deep-sourced CO_2. Furthermore, this study reveals that the Total Dissolved Inorganic Carbon (TDIC) in cold waters results from mixing between a shallow and a deeper carbon endmember that is equilibrated with carbonate lithology. In addition, the geochemical signature of TDIC in thermal carbon-rich water is explained by supplementary secondary processes, including equilibrium fractionation between solid, gas, and aqueous phases, as well as sinks such as mineral precipitation and CO_2 degassing. These findings have important implications for developing effective monitoring strategies for crustal fluids in different geological contexts and highlight the critical need to understand gas-water-rock interaction processes that control fluid

* Corresponding authors at: Istituto Nazionale di Geofisica e Vulcanologia, Sezione di Palermo, Palermo, 90146, Italy
E-mail addresses: dario.buttitta@ingv.it (D. Buttitta), antonio.caracausi@ingv.it acara@usal.es (A. Caracausi).

http://dx.doi.org/10.1016/j.scitotenv.2023.165367
Received 15 April 2023; Received in revised form 29 June 2023; Accepted 4 July 2023
Available online 9 July 2023

chemistry at depths that can affect the assessment of the CO_2 flux in atmosphere. Finally, this study highlights that the emissions of natural CO_2 from the seismically active Irpinia area are up to $4.08{\cdot}10^{+9}$ mol·y^{-1}, which amounts is in the range of worldwide volcanic systems.

1. Introduction

Deep sourced volatiles (e.g., He, CO_2) outgas extensively towards the atmosphere in active tectonic regions (Caracausi et al., 2005; Caracausi and Sulli, 2019; Chiodini et al., 2011; Chiodini et al., 2004; Italiano et al., 2009; Italiano et al., 2005; Randazzo et al., 2021; Tamburello et al., 2018) and this physical process can be explained by considering that tectonic discontinuities are regions of enhanced porosity and permeability through which volatiles can advectively move within the crust (Caracausi et al., 2022; Curzi et al., 2021). The nucleation of earthquakes is significantly influenced by the buildup of gases under high pressure along fault lines (Chiodini et al., 2004; Miller, 2004). This observation highlights the importance of volatiles in triggering seismic activity. At the same time, the processes acting during fluids transfer through the crust and the earthquakes nucleation can modify the physico-chemical composition of fluids during their transfer to the surface through the damage zones (Coppola et al., 2021; Marchesini et al., 2022). Furthermore, large changes in fluid migration rate can result from tiny alterations in rock, like small-scale heterogeneities (Krishnamurthy et al., 2022). In particular, the contrast in grain sizes can limit migration rates and increase the volumes of trapped fluids by 10^1–10^2 times (Krishnamurthy et al., 2022).

In active tectonic regions (e.g., Apennines, Italy) the roles of fluids are also supported by geophysical investigations that recognize 1) the presence of fluids in correspondence of the fault planes of seismogenetic faults (Piana Agostinetti et al., 2017), 2) the overpressure of fluids at depth able to generate aftershocks (Miller, 2004) and 3) groundwater recharge/circulation in modulating crustal deformation and seismicity (D'Agostino et al., 2018; Groppo et al., 2022). These evidences suggest to pose great attention also to the study of paleo-fluids trapped in minerals and veins along the faults (Curzi et al., 2023; Curzi et al., 2021; Marchesini et al., 2022; Smeraglia et al., 2018), to investigate the physico-chemical processes occurring at microscale along the fault planes and the adjacent regions (e.g., the damage zones) over time and to infer the characteristics of processes controlling the chemistry of fluids along faults prone to generate high magnitude earthquakes.

Two decades of geochemical investigations in seismically active regions (Barberio et al., 2017; Buttitta et al., 2020; Caracausi et al., 2005; Caracausi and Paternoster, 2015; Chiodini et al., 2020; Chiodini et al., 2011; Chiodini et al., 2004; Chiodini et al., 2000; Italiano et al., 2001; Tamburello et al., 2018) shown us the variation of geochemical parameters was observed in correspondence of moderate and high magnitude ($M > 5$) earthquakes. Hence, some relationships between the fluids transfer through the crust and seismicity at regional scales were hypothesized, but so far not clear and repeatable constraints of cause-effect over time have been still demonstrated. Consequently, the geochemical monitoring of natural fluids in seismic regions are crucial for understanding processes related to catastrophic earthquakes. A powerful use of fluids as tracers of seismogenic processes, needs detailed studies of physico-chemical processes controlling the fluids chemistry along faults prone to generate high magnitude earthquakes.

For instance, it is well recognized that outgassing of deep sourced volatiles occurs in active seismic regions, e.g. Tamburello et al., 2018, and tectonic discontinuities play as efficient networks of pathways for the groundwater circulation. Therefore, groundwater in shallow crustal layers intercepts the deep volatiles, crustal or mantle (Chiodini et al., 2000; Kipfer et al., 2002). Non-reactive volatiles (i.e., the noble gases) are directly transported to the surface (Aggarwal et al., 2015), while the reactive ones (e.g., CO_2), once dissolved in water are speciated (e.g., carbonate equilibrium) and their amounts and isotopic composition are modified by water-gas-rock interactions and solute precipitation (Gilfillan et al., 2009; Karolytė et al., 2019; Randazzo et al., 2021). Furthermore, when internal reworking predominates, the deep crustal carbon's source may have changed over time (Nicoli et al., 2022). In this scenario, the emerging groundwater carries traces of the processes at depth (e.g., mixing, water-gas-rock interaction). Hence, to figure out the processes at depth that control the chemistry of the fluids emitted at the surface, it is useful to develop physico-chemical models based on different geochemical tools (e.g., volatiles outputs, water chemistry, dissolved gases in water, isotopic geochemistry).

This study presents the main findings of a research focused on the gas-water-rock interaction and on C vs $\delta^{13}C_{TDIC}$ relationship in the thermal basin of Contursi and the surrounding areas of the Southern Apennine (Fig. 1, Italy), which is mainly based on the TDIC vs $\delta^{13}C_{TDIC}$ relationship. The area is located in a sector of the Apennine characterized by extensional tectonics and seismicity (Caracausi et al., 2022). In 1980, a catastrophic earthquake ($Ms = 6.9$) occurred in the region, and over the past ten years, the seismic activity in this area is characterized by small magnitude earthquakes ($M \leq 4.4$) (source: https://www.epos-eu.org/tcs/near-fault-observatories; Caracausi et al., 2022 and references therein). Previous studies also link CO_2 accumulation in crustal reservoirs to regional seismicity and suggest that dissolution/precipitation and subsequent outgassing processes regulate seismic activity and reduce powerful earthquakes (Klein et al., 2022). It is also worth mentioning that this area is characterized by high output of deep CO_2 (Chiodini et al., 2004) and mantle derived helium (Caracausi et al., 2013; Caracausi and Paternoster, 2015; Italiano et al., 2000).

This region hosts also the Mefite D'Ansanto gas emission, which is considered the largest no-volcanic emission of CO_2 (2000 tons·day^{-1}, Chiodini et al., 2010), and where the He isotopic signature in the released gases overlaps those in fluids outgassing at Vesuvio and Phlegrean Fields (Caracausi et al., 2022; Caracausi and Paternoster, 2015) volcanoes. Geophysical studies conducted in the Irpinia region reveal the existence of fluids along the seismogenic faults in the area (Amoroso et al., 2014). Despite the substantial release of deep CO_2 at the surface, its source remains uncertain and not well-defined, encompassing possibilities such as mantle/magmatic origins or decarbonation processes. However, through geochemical and petrological investigations, the presence of a carbon-rich regional mantle is identified (Bragagni et al., 2022; Carnevale et al., 2022).

In this study, the investigation on the origin of CO_2 at a regional scale, and the on gas-water-rock interaction, governing both the carbon abundances and isotopic composition in the groundwater, is carried out. A geochemical model to describe the fate of deep inorganic carbon from its source to the atmosphere is proposed. An accurate interpretation of the observed geochemical variations can help in choosing the parameters to be monitored in a future regional geochemical monitoring of seismic areas.

Finally, the evaluation of these processes can also has a notable impact on the assessments of the contribution of non-volcanic areas to the atmospheric CO_2 budget.

2. Structural setting of southern Apennines and seismicity

The configuration of the Southern Apennines is linked to the Meso-Cenozoic geotectonic mechanisms that implicated the African and European lithospheric plates. Various geotectonic stages including rifting, drifting, and compressive events ensued, resulting in the Apennines orogenic belt acquiring an *E*-NE vergence, duplex geometry, and out-of-sequence thrusting. These deformation features were primarily induced by orogenic contraction, which persisted from the upper Eocene-Oligocene Miocene until the late Pliocene, as documented by Cavazza et al., 2012.

In the study area (Fig. 1), the lithostratigraphy can be described in a top-to-bottom sequence of four units: (1) post-orogenic basin units within the

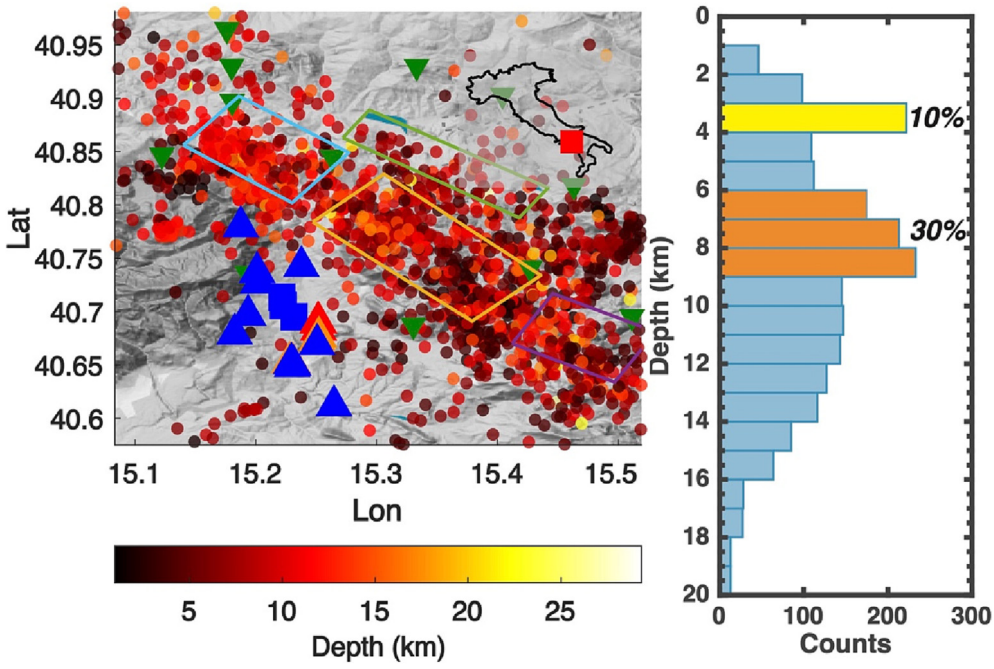

Fig. 1. Sampling sites and distribution of seismicity in Irpinia fault zone (Southern Italy). (a) Location of sampled cold waters (blue triangles), thermal and hypothermal water (red and orange triangles respectively) and free gases (blue squares) in the Contursi area and seismicity recorded by ISNet (inverted green triangles) during the years 2009 through 2019 (http://isnet-bulletin.fisica.unina.it/cgi-bin/isnet-events/isnet.cgi). Projection of seismogenic sources: Cervialto fault (light blue line), Marzano fault (yellow line), S. Gregorio fault (purple line) and Ofanto fault (green line). (b) Bimodal distribution of n° of earthquakes using Zmap7 (Wiemer, 2001) in The MathWorks Inc., 2022 software is identified. In the Irpinia fault zone the 10 % of seismicity is located between 3 and 4 km (yellow bar), roughly the bottom of the shallow reservoir, and the 30 % of seismicity is located between 6 and 9 km (orange bars), roughly the top of deeper reservoir. Shallow seismicity is characterized by $M \leq 3$, while the most intensive seismicity in the area ($4 \leq M \leq 4.4$) is located between 6 and 12 km coinciding with the gas-pressurized rock volumes developed under the Apulia Platform. More information on the lithologies of the area can be found in Gori et al., 2023.

intramountain region of marine, terrestrial, and volcanic origin. These were deposited during the Plio-Pleistocene or Holocene periods in the foredeep of the Adriatic-Bradanic basin. (2) Syntectonic sedimentary successions in the top-thrust basin formed during progressive compression towards the east. (3) Orogenic wedge tectonic units involved in NE-verging overthrusting from upper, internal domains, such as Tethyan oceanic crust or Adriatic-Apulian continental crust, to lower, external domains, including Apennine carbonate platforms with inter-basins pelagic units. (4) Apulian carbonates that are buried, deformed, and overthrust in the inner belt but are undeformed in the outcropping foreland. These findings have been previously documented by (Boncio et al., 2007) and (Patacca and Scandone, 2007).

Ascione et al., 2013 demonstrates that the Southern Apennine thrust belt has experienced extensional tectonics, with NW-SE oriented normal faults dissecting the area since the Quaternary period. This is confirmed through analysis of surface geology, borehole breakout, and fault plane solutions of earthquakes. The extension rate is estimated to be within the range of 3–5 $mm{\cdot}y^{-1}$.

Historically, the Southern Apennines have been subjected to earthquakes of X-XI MCS intensity, rendering them among the most seismically hazardous areas in the Mediterranean region. The presence of segmented, seismogenic structures in this region can potentially generate earthquakes of magnitude up to M 7. Typically, large earthquakes in this region initiate within the first 10–15 km of the crust and occur at recurrence intervals of $\geq$1000 years. Ghisetti and Vezzani, 2002 observe that the normal faults that dissect the Apennines demonstrate an evolutionary trend, progressing from young, high-angle planar faults situated in the upper crust, with limited extensional strains, to mature, listric faults that extend to the crystalline basal detachment with a high degree of extensional strain. The origin of large earthquakes within this tectonic context is also associated with the presence of fluids within the crust, which can lead to over-pressure conditions at depths of approximately 10 km due to the low permeability of the rock formations that inhibit their circulation (Improta et al., 2014).

The earthquake that struck Irpinia in 1980, measuring a magnitude of 6.9 on the Richter scale, took place along normal faults that trended in a northwest to southeast direction. It documented as the most destructive earthquake to have been recorded instrumentally in the Southern Apennines. The event was marked by a complicated rupture process, encompassing a number of fault segments, as documented by Pantosti and Valensise (1993).

Subsequent to the occurrence of the 1980 earthquake in Irpinia, the region has not experienced any other large-scale seismic events. Present-day seismic activity is marked by low-magnitude seismicity, with hypocentral depth mainly confined to within 15 km. Analysis of fault plane solutions reveals the predominance of normal and normal-strike slip kinematics, corroborating the prevailing SW-NE extensional regime, as documented by Festa et al., 2021. The underlying low-magnitude seismicity appears to be diffused over an extensive volume, as illustrated in Fig. 1, with the related stress field closely linked to the primary fault segments activated during the 1980 Irpinia earthquake. Furthermore, the occurrence of microseismicity seems to be regulated by the elevated pore pressure of water-saturated Apulian carbonates present within a fault-bounded crustal volume, as reported by D'Agostino et al., 2018, De Landro et al., 2022; Picozzi et al., 2022. The existence of crustal fluids constitutes a significant factor that must be accounted for in hazard assessments, given the strong correlation observed between seismicity and high-fluid pressure during recent severe earthquakes in the Apennines, such as the Mw 6.0, 1997 Colfiorito earthquake, and the Mw 6.3, 2009 L'Aquila earthquake.

According to Improta et al., 2014 tomographic imaging of the Irpinia region reveals two distinct types of reservoirs. The first is a dome-shaped body with low Vp/Vs ratios, measuring 20 km in length and 15 km in width, located between 7 and 13 km beneath Mount Forcuso in the northern region of Irpinia. This geophysical data is indicative of a CO_2-rich rock volume that is deeply situated and pressurized, likely filled beneath the Apulian platform carbonates by fluid-rich mantle melts that have intruded into the crust. This anomaly is consistent with the high values of heat flow (100–215 $mW{\cdot}m^{-2}$) observed along the Mount Forcuso antiform, and with

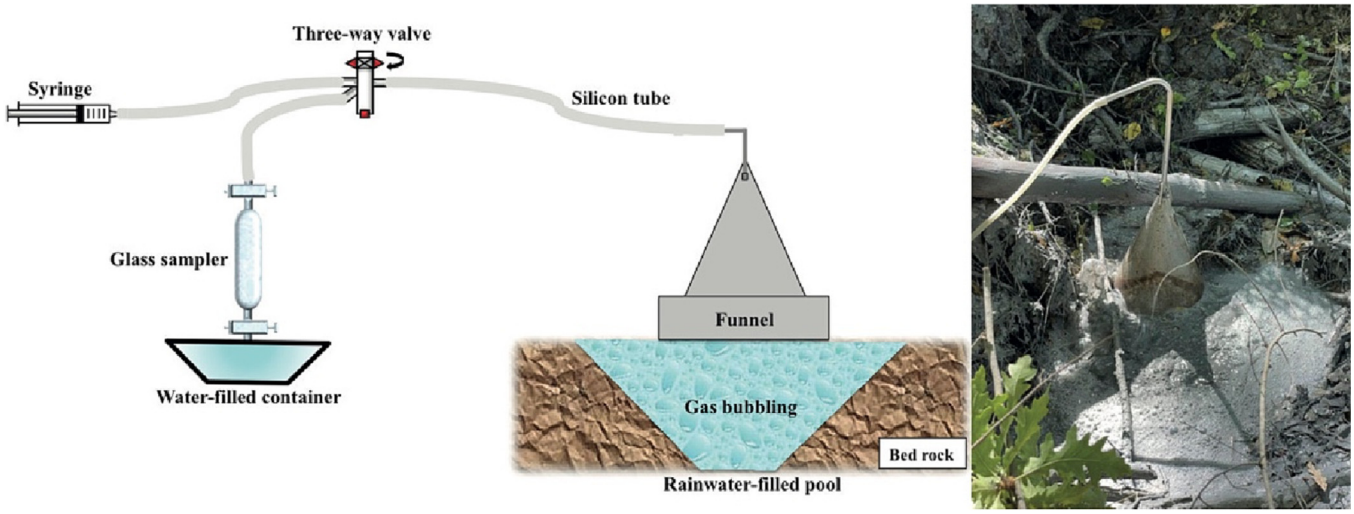

Fig. 2. Schematic illustration showing the sampling system used for collecting the free gaseous manifestations. Modified from Ventura Bordenca, 2020.

geochemical data. In the central portion of Irpinia, roughly within the Marzano segment where the 1980 earthquake was generated, tomographic images (Improta et al., 2014) demonstrate a broad region with high Vp/Vs ratios between 1 km and 4 km, which is interpreted as fractured, fluid-saturated carbonates.The physical modeling of 3D velocity images (Amoroso et al., 2017) lead to estimate a porosity of carbonates in the Marzano segment around 4–5 % and a fluid composition consisting of brine–CO_2 and/or CH_4 –CO_2. The occurrence of pressure changes in fluid-filled cracks within carbonates is considered one of the main trigger mechanisms of microearthquakes in the Irpinia region.

The Contursi hydrothermal system is located in the Sele river valley, situated between the two fault segments of Marzano (where the 1980 earthquake originated) and Cervialto. According to Cocco and Pacor, 1993 the rupture evolution that took place during the 1980 Irpinia earthquake indicates a gap in the slip distribution precisely corresponding to the Sele Valley. In addition, Caracausi et al., 2022 observe an high b-value of the Gutenberg-Richter frequency magnitude distribution for the Sele river valley sector, indicating the presence of fluids that may influence microseismic activity. This sector may function as an extensional transfer zone between the Marzano and Cervialto fault segments, a tectonic phenomenon that is still under investigation but is consistent with the presence of the Contursi hydrothermal system.

3. Sampling and analytical procedures

During the period between 2021 and 2022, a sampling campaign is carrier out to collect hot and cold waters from natural springs and wells in the thermal basin of Contursi and its surrounding areas. Additionally, two free gases, namely S. Sisto (SST) and Oliveto Citra 1–2 (OV1–2), were collected from high flux CO_2 gas emissions, as shown in Figs. 1a and 2, and listed in Table 1. To prevent air contamination, a steel funnel, a three-direction valve, and a syringe were employed to collect gaseous samples in pyrex bottles equipped with vacuum valves at both ends, as illustrated in Fig. 2.

Table 1
Physical data of groundwater from the study area. Q is a water flow rate in $L{\cdot}s^{-1}$. The —S notation in Sample ID, correspond to the number of springs reported in Gori et al., 2023.

	Sample name	Sample ID	Sampling date	Latitude	Longitude	T (°C)	EC ($\mu S{\cdot}cm^{-1}$)	pH	Eh (mV)	Q ($L{\cdot}s^{-1}$)	TDS ($mg{\cdot}L^{-1}$)
Cold waters	Acquara Ponticchio	AQP-S1	03/05/2021	15.188	40.780	7.8	354	7.8	272.4	100	224.9
	Piceglia Alta	PSA-S2	03/05/2021	15.201	40.737	7.9	300	7.7	252.7	–	191.6
	fiumicello	FIU-S3	03/05/2021	15.202	40.727	9.7	298	8.4	206.5	40	180.6
	S. Oronzo	SRON-S5	03/05/2021	15.194	40.697	10.1	352	7.8	301.8	20	222.3
	Senerchiella	SEN-S4	03/05/2021	15.238	40.742	10.5	518	7.4	298.7	2000	306.6
			24/01/2022			10.6	514	7.4			
	Magliana	MAG-S6	03/05/2021	15.182	40.679	12.1	398	7.5	178.3	10	259.9
	Sorgente la Regina	REG-S7	03/05/2021	15.265	40.612	12.8	664	7.2	299.0	5590	400.9
			24/01/2022			12.9	680	7.2			
Hypothermal waters	Acetosella	ACT-S14	03/05/2021	15.231	40.650	13.8	1054	6.8	198.0	5	719.2
	Don Carlo	DC-S9	03/05/2021	15.230	40.649	14.1	1090	6.5	85.8	50	722.4
	Fontana Prete	FP-S8	03/05/2021	15.251	40.670	14.3	613	7.5	166.3	0.1	380.5
	Cantani Mix	CAM-S13	03/05/2021	15.229	40.651	14.4	1298	6.6	213.6	70	872.0
	Ferrata	FR-S11	04/05/2021	15.229	40.652	14.7	1435	6.5	228.9	0.7	986.8
	Cantani Solfurea	CAS-S10	04/05/2021	15.228	40.653	17.3	1981	6.1	−197.3	100	1436.3
	Forlenza	FOR-S12	05/05/2021	15.230	40.652	18.5	19,824	6.3	−147.8	500	1403.4
	Tufaro	TUF-S17	04/05/2021	15.251	40.674	24.8	2770	6.2	−197.5	–	2112.3
	Cappetta Nuova	CAN-S16	04/05/2021	15.252	40.676	26.4	2560	6.3	−219.2	–	1964.4
	Cappetta Vecchia	CAV-S15	04/05/2021	15.252	40.676	26.4	2570	6.3	−224.5	50	1813.1
	Capasso Venere	VEN-S20	05/05/2021	15.251	40.690	34.3	5240	6.2	−273.9	–	4020.6
	Rosa Pepe Fredda	RSF-S18	04/05/2021	15.185	40.683	36.8	4460	6.2	−273.2	60	2628.0
	Rosa Pepe Calda	RSC-S19	04/05/2021	15.185	40.683	37.5	4640	6.3	−258.5	40	3324.1
			24/01/2022			38.4	4640	6.2			
Thermal waters	Capasso Geyser	GEY-S21	04/05/2021	15.251	40.690	46.4	6380	6.4	−285.0	13	4345.1
			24/01/2022			48.4	6520	6.4			
	Capasso Ercole	ERC-S22	05/05/2021	15.252	40.690	47.0	6470	6.4	−263.0	–	49.51.8
			24/01/2022			49.0	6430	6.4			

The chemical (O_2, N_2, CH_4, He, and CO_2) and isotopic composition of both dissolved and free gases in water were analyzed. The analysis was carried out at the Istituto Nazionale di Geofisica e Vulcanologia (INGV—Palermo) to determine the characteristics of the gases. The dissolved and free gases were analyzed using a Perkin Elmer Autosystem XL gas chromatograph equipped with a double detector (TCD-FID), a 4 m Carboxen 1000 column, and Ar as the carrier gas. The analytical errors for CO_2, N_2, H_2, CO, CH_4, and O_2 do not exceed 3 %. The method utilized for the analysis of dissolved gases was proposed by Capasso and Inguaggiato, 1998.

The isotopic ratio $^3He/^4He$ and ^4He were measured by a split-flight-tube mass spectrometer (GVI Helix SFT) equipped with a double collector system that enabled simultaneous detection of ion beams after purification of the sample from the major gaseous species and separation from the other noble gases. The precision of the isotopic ratio measurement is within ±0.5 %, using purified atmospheric helium as a standard. A multicollector Thermo-Helix MC Plus mass spectrometer is being utilized to measure ^{20}Ne, after purification procedure into a stainless steel ultra-high vacuum line distinct from that of He and following cryogenic trap purification. Further details on samples purification and analysis are described by Rizzo et al., 2019.

$\delta^{13}C_{TDIC}$ was determined, following the method descripted in Capasso et al., 2005b through chemical and physical stripping of CO_2 by adding 150–200 μL of 100 % H_3PO_4. The isotopic values were analyzed using a Thermo Delta V Plus isotope ratio mass spectrometer coupled to a GasBenchII and reported in δ‰ versus V-PDB standard, with a standard deviation of $^{13}C/^{12}C$ ratio of ±0.15 ‰.

The methodology employed to determine the chemical-physical parameters, major ions, minor and trace elements, as well as saturation indices, is documented in Gori et al., 2023.

4. Results

In this study, a total of twenty-three springs and two free gas emissions were examined (as depicted in Fig. 1a). The locations, temperatures, pH values, and groundwater major ions present in the water are provided in Table 1. Additionally, Table 2 includes the chemical composition of the free gases and dissolved gases in the groundwater, along with the isotopic composition of carbon and helium.

4.1. Bulk gas concentrations, $\delta^{13}CO_2$ water measurements and noble gas data

All gas samples from thermal (34.3 < T°C < 49) and hypothermal (17.3 < T°C < 26.4) springs are CO_2 dominant with less amount of N_2 (from 1.10 to 8.66 ccSTP·L^{-1}) and O_2 (from 0.04 to 0.16 ccSTP·L^{-1}). In the cold springs (T < 15 °C) CO_2 is the major constituent (up to 141.02 ccSTP·L^{-1} for DC site), except for PSA-S2 and SEN-S4 sites having the highest nitrogen amounts (19.93 and 17.37 ccSTP·L^{-1}, respectively). All water samples were found to contain trace amounts of CH_4 (from $1.25{\cdot}10^{-5}$ to $8.56{\cdot}10^{-2}$ ccSTP·L^{-1}), CO (from $1.73{\cdot}10^{-5}$ to $7.94{\cdot}10^{-4}$ ccSTP·L^{-1}). The pH values in Table 1 vary between 6.1 and 8.4, and the total dissolved solid (TDS) values were measured to range from 180.6 to 4951.8 mg·L^{-1}. The $\delta^{13}C_{TDIC}$ value in the cold water ranges from −14.71 to −1.74 ‰. In the thermal and hypothermal waters this value is positive and ranges from 0.47 to 3.67 ‰ (see Table 2).

CO_2 concentrations measured in the free gases sites (OV1–2 and SST) range from 94.86 % to 96.92 %, with the residual gas that are predominantly made of N_2 (up to 3.5 %), O_2 (up to 0.15 %), and with traces of CH_4 and CO (up to 0.39 % and up to 1 ppm, respectively).

At twelve sites, the abundances of elemental and isotopic ratios of He and the measurement of $^4He/^{20}Ne$ were determined. In cold and hypothermal waters, the He contents range from $1.71{\cdot}10^{-4}$ to $9.70{\cdot}10^{-4}$ ccSTP·L^{-1}, in thermal waters range from $2.57{\cdot}10^{-5}$ to $3.88{\cdot}10^{-5}$ ccSTP·L^{-1} and in the free gases range from 17.30 to 25.00 ppm. (see Table 2).

The reported He isotopic ratios $^3He/^4He$ are normalized to the value of air (where 1 Ra is the atmospheric ratio of $1.382 \pm 0.005{\cdot}10^{-6}$, Mabry et al., 2013). The latter ranges in the study area from 0.64 (RSF-S18) to 1.40 (SEN—S4).

The mantle, atmosphere, and crust are the three primary sources from which the origin of helium in natural fluids can be traced (Ballentine and Sherwood Lollar, 2002). Considering that the mixing processes between

Table 2
Chemical and isotopic composition ($\delta^{13}C$ and $^3He/^4He$) of the dissolved and free gases. The analytical uncertainty is <3 % for chemical analysis, below 0.3 % for He and Ne and 0.1 % for C isotope composition. In the free gase samples, He isotopic ratio is corrected for the contribution of atmospheric He and reported as Rc/Ra, by using the approach proposed by (Sano et al., 1987). The Rc/Ra of free gas sites range from 1.27 ± 0.01 (OV1) to 1.41 ± 0.01 (SST). For the dissolved samples, the elementary ratio $^4He/^{20}Ne$ is <3. In this case, the Rc/Ra differ significantly from the measured $^3He/^4He$ ratios which would make the correction erroneous (according to Sano et al., 2006) therefore its $^3He/^4He$ values are reported uncorrected and range from 0.64 (RSF-S18) to 1.40 (SEN—S4) Ra.

Type	Sample ID	He (ccSTP·L^{-1})	H_2 (ccSTP·L^{-1})	O_2 (ccSTP·L^{-1})	N_2 (ccSTP·L^{-1})	CO (ccSTP·L^{-1})	CH_4 (ccSTP·L^{-1})	CO_2 (ccSTP·L^{-1})	$\delta^{13}C_{TDIC}$	$\frac{^4He}{^{20}Ne}$	$\frac{^4He}{^3He}(Ra)$	$\frac{Rc}{Ra}$
Dissolved	AQP-S1								−11.44			
	PSA-S2	b.d.l.	$1.51{\cdot}10^{-3}$	8.52	19.93	$3.54{\cdot}10^{-5}$	$6.55{\cdot}10^{-5}$	2.28	−10.42			
	SEN-S4	$2.22{\cdot}10^{-4}$	$1.35{\cdot}10^{-4}$	7.19	17.37	$2.06{\cdot}10^{-5}$	$1.25{\cdot}10^{-5}$	14.90	−5.65			
		$2.27{\cdot}10^{-4}$	$1.87{\cdot}10^{-3}$	5.76	12.05	b.d.l.	b.d.l.	14.03		1.07	1.40	
	REG-S7	$4.45{\cdot}10^{-4}$	b.d.l.	5.10	19.16	b.d.l.	$3.29{\cdot}10^{-5}$	25.44	−4.72			
		$9.70{\cdot}10^{-4}$	$1.90{\cdot}10^{-3}$	3.86	14.44	b.d.l.	$4.53{\cdot}10^{-5}$	27.61	n.d.	3.53	1.32	
	DC-S9	$1.71{\cdot}10^{-4}$	$1.94{\cdot}10^{-4}$	4.09	10.07	$2.08{\cdot}10^{-5}$	$2.42{\cdot}10^{-5}$	141.02	−1.74			
	FP-S8	b.d.l.	$1.64{\cdot}10^{-4}$	4.38	15.63	$2.63{\cdot}10^{-5}$	$2.61{\cdot}10^{-4}$	21.58	−14.71			
	CAS-S10	$2.91{\cdot}10^{-4}$	b.d.l.	0.07	8.66	b.d.l.	$8.56{\cdot}10^{-2}$	557.93	0.47	1.51	1.07	
	FOR-S12	b.d.l.	b.d.l.	0.04	2.87	b.d.l.	$8.58{\cdot}10^{-3}$	546.70	1.52			
	TUF-S17	b.d.l.	b.d.l.	0.06	2.27	b.d.l.	$1.33{\cdot}10^{-2}$	595.07	2.02			
	CAN-S16	b.d.l.	b.d.l.	0.09	4.59	$1.73{\cdot}10^{-5}$	$3.70{\cdot}10^{-3}$	471.26	2.18	0.49	0.87	
	VEN-S20	b.d.l.	b.d.l.	1.87	$2.63{\cdot}10^{-4}$	$7.94{\cdot}10^{-4}$	578.22	3.67	n.d.			
	RSF-S18	b.d.l.	$1.32{\cdot}10^{-4}$	0.10	4.81	$4.71{\cdot}10^{-5}$	$2.87{\cdot}10^{-4}$	403.60	3.63	0.63	0.64	
	RSC-S19	b.d.l.	$3.21{\cdot}10^{-4}$	0.12	1.60	b.d.l.	$1.46{\cdot}10^{-3}$	1096.29	n.d.			
		$2.57{\cdot}10^{-5}$								0.53	0.91	
	GEY-S21	b.d.l.	$5.60{\cdot}10^{-4}$	0.10	3.02	$5.10{\cdot}10^{-5}$	$1.73{\cdot}10^{-3}$	459.47	3.55	0.42	0.95	
		$3.88{\cdot}10^{-5}$	$9.33{\cdot}10^{-4}$	0.16	2.80	b.d.l.	$1.51{\cdot}10^{-3}$	951.96	n.d.	0.51	0.90	
	ERC-S22	b.d.l.	$7.78{\cdot}10^{-4}$	0.12	4.22	b.d.l.	$1.43{\cdot}10^{-4}$	492.44	3.02			
		b.d.l.	$1.20{\cdot}10^{-3}$	0.15	1.10	$1.44{\cdot}10^{-4}$	$4.63{\cdot}10^{-5}$	1007.87	n.d.	0.53	0.84	
		He (ppm)	**H_2 (ppm)**	**O_2 (%)**	**N_2 (%)**	**CO (ppm)**	**CH_4 (%)**	**CO_2 (%)**	**$\delta^{13}C_{CO_2}$**	$\frac{^4He}{^{20}Ne}$	$\frac{^4He}{^3He}(Ra)$	$\frac{Rc}{Ra}$
Free	OV1	22.55	31	0.1	3.35	0.5	0.37	95.32	0.86	215.16	1.27	1.27
		25.00		0.15	3.31		0.39	94.86		263.68	1.28	1.28
	OV2	20.00	92	0.04	2.39	1	0.33	95.69	n.d.	284.44	1.28	1.28
	SST	17.30	98	0.12	2.65		0.29	96.92	0.70	48.66	1.41	1.41

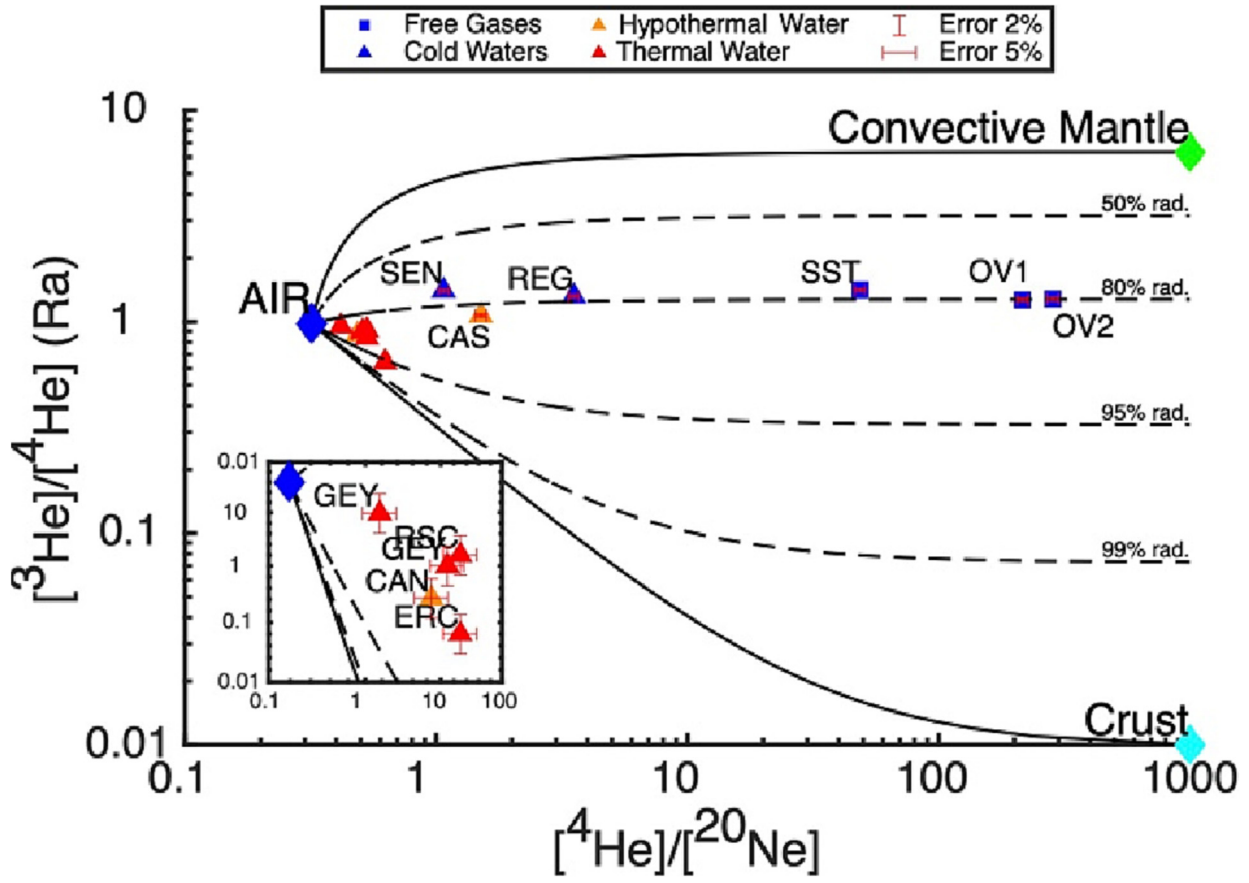

Fig. 3. A correlation diagram between the $^{3}He/^{4}He$ and $^{4}He/^{20}Ne$ ratios for the springs and free gases investigated. Solid lines depict binary mixing between air ($^{3}He/^{4}He$ = 1 Ra, $^{4}He/^{20}Ne$ = 0.319 Ozima and Podosek, 2002), the Sub Continental Lithospheric Mantle, SCLM, ($^{3}He/^{4}He$ = 6.32 ± 0.39 Ra, Gautheron et al., 2005, $^{4}He/^{20}Ne > 10^{3}$, Sano and Wakita, 1985), crustal end-member ($^{3}He/^{4}He$ = 0.01–0.05 Ra, Halford et al., 2022, $^{4}He/^{20}Ne > 10^{3}$, Ozima and Podosek, 2002). In the main figure the errors are smaller than the symbols.

these three components control the He isotopic ration in the natural fluids, a useful approach for discriminating their contributions is to solve the mixing equations based on the $^{3}He/^{4}He$ and $^{4}He/^{20}Ne$ ratios (Sano and Wakita, 1985), Fig. 3.

In the free gas samples collected in Irpinia, the $^{4}He/^{20}Ne$ ratios range from 48.66 in the San Sisto site to 284.44 in OV1–2 site (see Table 2). These values greatly exceed (by 153–892 times) the $^{4}He/^{20}Ne$ expected for atmospheric value (0.319, Ozima and Podosek, 2002), suggesting that the collected samples have a negligible amount of atmospheric helium (<0.6 %). In contrast, the highest $^{4}He/^{20}Ne$ ratio is found in the dissolved gases in water, with values equal to 3.54, which is 12 times the ratio in air-saturated water ASW = 0.285 at 25 °C (Ozima and Podosek, 2002). The low $^{4}He/^{20}Ne$ ratio of the dissolved gases (Fig. 3) indicates that they are dominated by the atmospheric component. In fact, the $^{4}He/^{20}Ne$ ratios are not resolvable from atmospheric ones. It is noteworthy that the lowest $^{4}He/^{20}Ne$ ratios are found in thermal water samples (RSF-S18, RSC-S19, GEY—S21, ERC—S22). The free gas in the area (SS and OV1–2), are characterized by a strong crustal component (about the 80 %), while only the remaining 20 % is related to the mantle component (in the caption of Fig. 3 all the details about the used mantle endmember). The elevated atmospheric contamination of He in the groundwater does not allow realistic assumptions about the origin of He and the associated dissolved gases in these waters to be made.

The combination of the CO_2 amount, its carbon isotopes ($\delta^{13}C_{CO2}$) and He in natural fluids is a widely employed approach to detect the occurrence of mantle-derived volatile compounds, even at considerable distances from both active and quiescent volcanic systems (Randazzo et al., 2022; Randazzo et al., 2021). It is worth to remember that ^{3}He in natural fluids is not largely produced in the crust, while in contrast, ^{4}He is continuously produced there by the U and Th decay. Hence, low $^{3}He/^{4}He$ ratios (typically 0.01 or 0.02 Ra, Halford et al., 2022), and $CO_2/^{4}He$ ratios $>1.4{\cdot}10^{+2}$, are usually associated with a crustal CO_2 source (Halford et al., 2022). In a $CO_2/^{4}He$ vs $^{4}He/^{3}He$ (Ra) plot (Fig. 4), our samples are fitted along a mixing line between the Sub Continental Lithospheric Mantle (SCLM) and a local crustal end-member. However, the observed dispersion

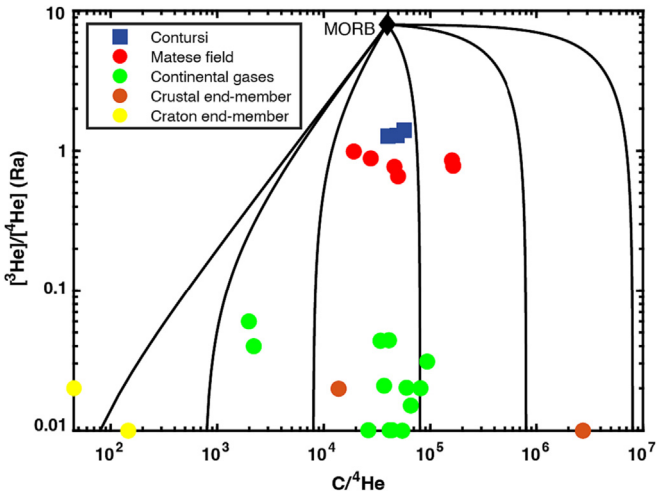

Fig. 4. Binary mixing plot between Mantle ($^{3}He/^{4}He$ = 8 Ra, $CO_2/^{4}He = 3.94{\cdot}10^{4}$, Marty et al., 2020) and various crustal end-members ($CO_2/^{4}He$ = 80–$8{\cdot}10^{6}$). The additional data are from INGV internal database.

Table 3
Results of aqueous speciation calculations and dissolved carbon. Calculated saturation indices for calcite, dolomite and gypsum and partial pressure of CO_2 gas, given as 10^{SI} atm.

Sample ID	^{SI}Calcite	^{SI}Dolomite	^{SI}Gypsum	$^{SI}CO_2(g)$	TDIC (mmol·L^{-1})
AQP-S1	0.46	−0.40	−2.96	−2.50	4.26
PSA-S2	0.24	−0.17	−3.20	−2.49	3.92
FIU-S3	0.84	1.21	−3.18	−3.21	3.46
SRON-S5	0.43	0.05	−2.95	−2.46	4.21
SEN-S4	0.29	−0.09	−2.69	−1.93	6.46
	0.23	−0.21	−2.69	−1.95	6.37
MAG-S6	0.35	−0.85	−2.69	−2.14	4.85
REG-S7	0.32	−0.02	−2.33	−1.66	8.15
	0.24	−0.19	−2.32	−1.66	8.16
ACT-S14	0.38	−0.02	−2.05	−1.02	17.10
DC-S9	0.10	−0.64	−2.05	−0.71	21.84
FP-S8	0.66	0.14	−2.18	−2.02	6.76
CAM-S13	0.29	−0.28	−1.89	−0.70	24.10
FR-S11	0.28	−0.27	−1.78	−0.58	28.57
CAS-S10	0.13	−0.47	−1.58	−0.06	59.80
FOR-S12	0.01	−0.63	−1.49	−0.26	43.05
TUF-S17	0.39	0.12	−0.88	−0.16	47.02
CAN-S16	0.40	0.17	−0.96	−0.16	46.00
CAV-S15	0.32	−0.02	−1.03	−0.17	44.68
VEN-S20	0.67	0.91	−0.63	0.10	69.68
RSF-S18	0.21	0.46	−1.13	−0.04	46.61
RSC-S19	0.82	1.23	−0.89	0.03	63.23
	0.68	0.94	−0.87	0.15	71.04
GEY-S21	0.57	1.31	−1.12	−0.14	40.84
	0.52	1.21	−1.10	−0.13	40.61
ERC-S22	1.00	1.83	−0.81	0.01	59.29
	0.95	1.75	−0.80	0.03	59.19

is probably due to the of effects such as loss of CO_2, assimilation of crustal ^{4}He (shift to the left), and/or addition of crustal CO_2 or degassing in open system, shift to the right, (Karolytė et al., 2019; Randazzo et al., 2021).

This suggests that the secondary processes associated with mixing are of considerable importance and warrant further investigation. In light of this, the upcoming sections of this study will be dedicated to a thorough examination of these processes.

4.2. Carbon mass balance of the aquifers as a simple mixing process

The classic simplified approach to determine the exogenous CO_2 amount, that once dissolved in the groundwater is transferred in the atmosphere, is based on a mixing process between a number of sources (such as dissolution of carbonate minerals, input of deeply derived CO_2, oxidation of organic material) combining the total inorganic carbon with the $\delta^{13}C_{TDIC}$.

The total carbon dissolved in groundwater, the saturation indices (SI) for calcite, dolomite, anhydrite, and gypsum, as well as the partial pressure of CO_2 gas for the springs, were calculated by combining their water chemistry, pH, HCO_3^-, and T (Gori et al., 2023). These calculations were done using the PHREEQC computer code (Parkhurst et al., 1980) and shown in Table 3.

In detail, according to Chiodini et al., 2000, Chiodini et al., 1999, the total carbon (C_{tot}) that moved through carbonate-aquifer is due to both carbonate dissolution inside the aquifer (C_{carb}) and contributions from sources external to the aquifer (C_{ext}).

The carbon mass balance equations are employed to evaluate the isotopic composition and quantify the respective contribution of various carbon sources for each sample, resulting in the computation of C_{ext} and $\delta^{13}C_{ext}$.

$$C_{tot} = C_{carb} + C_{ext} \quad (1)$$

and

$$\delta^{13}C_{tot}\ C_{tot} = \delta^{13}C_{carb}\ C_{carb} + \delta^{13}C_{ext}\ C_{ext} \quad (2)$$

where C_{tot} and $\delta^{13}C_{tot}$ corresponding to the Total Dissolved Inorganic Carbon-TDIC (calculated using PHREEQC) and $\delta^{13}C_{TDIC}$ (analytically determinate) respectively; Ccarb, is calculated as the sum of [Ca] + [Mg] considering the dissolution of carbonate minerals (i.e., calcite and dolomite) and setting the $\delta^{13}C_{carb}$ at 2.21 ‰ ± 0.66 ‰ (vs. PDB) as assumed in the Apennine aquifer from carbonate mineral dissolution (Chiodini et al., 2004). According to the approach proposed by Chiodini et al., 2020, by using the Eqs. (1) and (2), the C_{ext} and $\delta^{13}C_{ext}$ for water samples were computed in this study (Table 4).

Table 4
Output of Deep CO_2 in predegassing and post degassing condition. SST data from Italiano et al., 2000.

	Sample ID	Q (L·s^{-1})	TDIC (mmol·L^{-1})	C_{carb} (mmol·L^{-1})	C_{ext} (mmol·L^{-1})	C_{inf} (mmol·L^{-1})	C_{deep} (mmol·L^{-1})	Q_{CDeep} (mol·y^{-1})	$Q_{CDeep\text{-}Pre\ Degassing}$ S = 0 ‰ (mol·y^{-1})	$Q_{CDeep\text{-}Pre\ Degassing}$ S = 35 ‰ (mol·y^{-1})
Cold Waters	AQP-S1	100	4.26	2.26	2.00	2.00	0.00			
	PSA-S2		3.92	1.80	2.12	2.12	0.00			
	FIU-S3	40	3.46	1.70	1.76	1.76	0.00			
	SRON-S5	20	4.21	2.20	2.01	2.01	0.00			
	SEN-S4	2000	6.46	2.92	3.54		1.23			
			6.37	2.92	3.46		1.15			
	MAG-S6	10	4.85	2.50	2.35		0.04			
	REG-S7	5590	8.15	3.75	4.40		2.09	$3.69{\cdot}10^{+8}$		
			8.16	3.75	4.41		2.10	$3.71{\cdot}10^{+8}$		
	ACT-S14	5	17.10	7.02	10.08		7.77	$1.23{\cdot}10^{+6}$		
	DC-S9	50	21.84	7.01	14.83		12.52	$1.98{\cdot}10^{+7}$		
	FP-S8	0.1	6.76	3.53	3.23		0.92	$2.90{\cdot}10^{+3}$		
	CAM-S13	70	24.10	8.43	15.67		13.36	$2.95{\cdot}10^{+7}$		
	FR-S11	0.7	28.57	9.50	19.06		16.75	$3.70{\cdot}10^{+5}$		
Hypothermal Waters	CAS-S10	100	59.80		59.80		57.49	$1.81{\cdot}10^{+8}$	$2.49{\cdot}10^{+8}$	$4.17{\cdot}10^{+8}$
	FOR-S12	500	43.05		43.05		40.74	$6.43{\cdot}10^{+8}$	$1.24{\cdot}10^{+9}$	$2.08{\cdot}10^{+9}$
	TUF-S17		47.02		47.02		44.71			
	CAN-S16		46.00		46.00		43.69			
	CAV-S15	50	44.68		44.68		42.37	$6.69{\cdot}10^{+7}$	$1.24{\cdot}10^{+8}$	$2.08{\cdot}10^{+8}$
	VEN-S20		69.68		69.68		67.37			
Thermal Waters	RSF-S18	60	46.61		46.61		44.30	$8.39{\cdot}10^{+7}$	$1.49{\cdot}10^{+8}$	$2.50{\cdot}10^{+8}$
	RSC-S19	40	63.23		63.23		60.92	$7.69{\cdot}10^{+7}$	$9.96{\cdot}10^{+7}$	$1.67{\cdot}10^{+8}$
			71.04		71.04		68.73	$8.68{\cdot}10^{+7}$	$9.96{\cdot}10^{+7}$	$1.67{\cdot}10^{+8}$
	GEY-S21	13	40.84		40.84		38.53	$1.58{\cdot}10^{+7}$	$3.24{\cdot}10^{+7}$	$5.42{\cdot}10^{+7}$
			40.61		40.61		38.30	$1.57{\cdot}10^{+7}$	$3.24{\cdot}10^{+7}$	$5.42{\cdot}10^{+7}$
	ERC-S22		59.29		59.29		56.98			
			59.19		59.19		56.88			
Free Gas	SST							$4.82{\cdot}10^{+8}$		

In turn, C_{ext} represents the carbon content of infiltrating waters (C_{inf}; i.e. atmospheric CO_2 plus carbon from biogenic sources active in the soils during infiltration) and the carbon content of deep sources (C_{deep}) (Frondini et al., 2019):

$$C_{ext} = C_{inf} + C_{deep} \quad (3)$$

from which result the following mass balance:

$$\delta^{13}C_{ext} = \frac{\delta^{13}C_{inf} \cdot C_{inf} + \delta^{13}C_{deep} \cdot C_{deep}}{C_{ext}} \quad (4)$$

The used equations can underestimate the Cext and enriching δ^{13}Cext values, if the water is significantly affected by CO_2 degassing and/or carbonate minerals precipitation because of the significant isotopic fractionation. According to Chiodini et al., 2011, these effects are assumed to be negligible in samples with TDIC<40 mmol·L^{-1} (equivalent to 30 mmol·L^{-1} of Cext). Hence, according to such "CO_2 degassing threshold", the system can be assumed conservative for carbon species and the dissolved carbon together with its isotopic composition can be considered the result of a simple mixing between different carbon sources (Chiodini et al., 2011).

The Fig. 5, shows that samples from cold water, specifically DC-S9, REG—S7, and SEN—S4, fall within the theoretical mixing field computed by adding varying amounts of C_{deep} with $\delta^{13}C_{deep}$ ranging from −1 to +1 ‰ to the infiltrating water. This field partially overlaps the typical range of deeply-derived CO_2 emitted in Italy by volcanoes, geothermal systems, and cold CO_2 emissions (−5 to +1 ‰) as reported by Chiodini et al., 2004. Conversely, cold water samplers PSA—S2, AQP-S1, and FP-S8 are characterized by low Cext values (<3 mmol/l) and extremely negative $\delta^{13}C_{ext}$ ranges from −21.10 to −33.24 ‰, and partially overlap the $\delta^{13}C_{ext}$ range of recharge waters of the Apennines, −21.6 ± 2.9 ‰ (Frondini et al., 2019). In these springs, the Cdeep is negligible and Cext actually matches Cinf. Our samples reach much negative values probably due to mixing with a strongly negative biogenic endmember, around −40 ‰, the typical value of hydrocarbon oxidation products (Holland and Gilfillan, 2012).

On the other hand, thermal and hypothermal waters, with Cext above the threshold, fall outside of the theoretical range of mixing with a deep endmember. For these samples, this approach considers the CO_2 signature unaffected by the gas-rock-water interaction outcome, which can modify the pristine isotopic signature. In the following sections, the reworking undergone by mantle/carbonate CO_2 in the deep reservoir due to the interaction with dolomite and the subsequent water-rock interaction in the shallower reservoir will be considered.

5. Discussion

In the following sections, an analysis will be presented of the data collected from the survey, alongside a discussion of the methodologies utilized for its processing. Hereinafter, the interactions between the CO_2-rock before and CO_2-rock-water after were modeled in the present study. During these interactions, degassing and precipitation processes occur, and the output due to free and dissolved gas emissions were quantified.

5.1. CO_2-rocks interactions in deep crustal layers

The largely used mixing model examined in the previous sections assumes that the outcome of the gas-rock-water interaction (except the carbonate

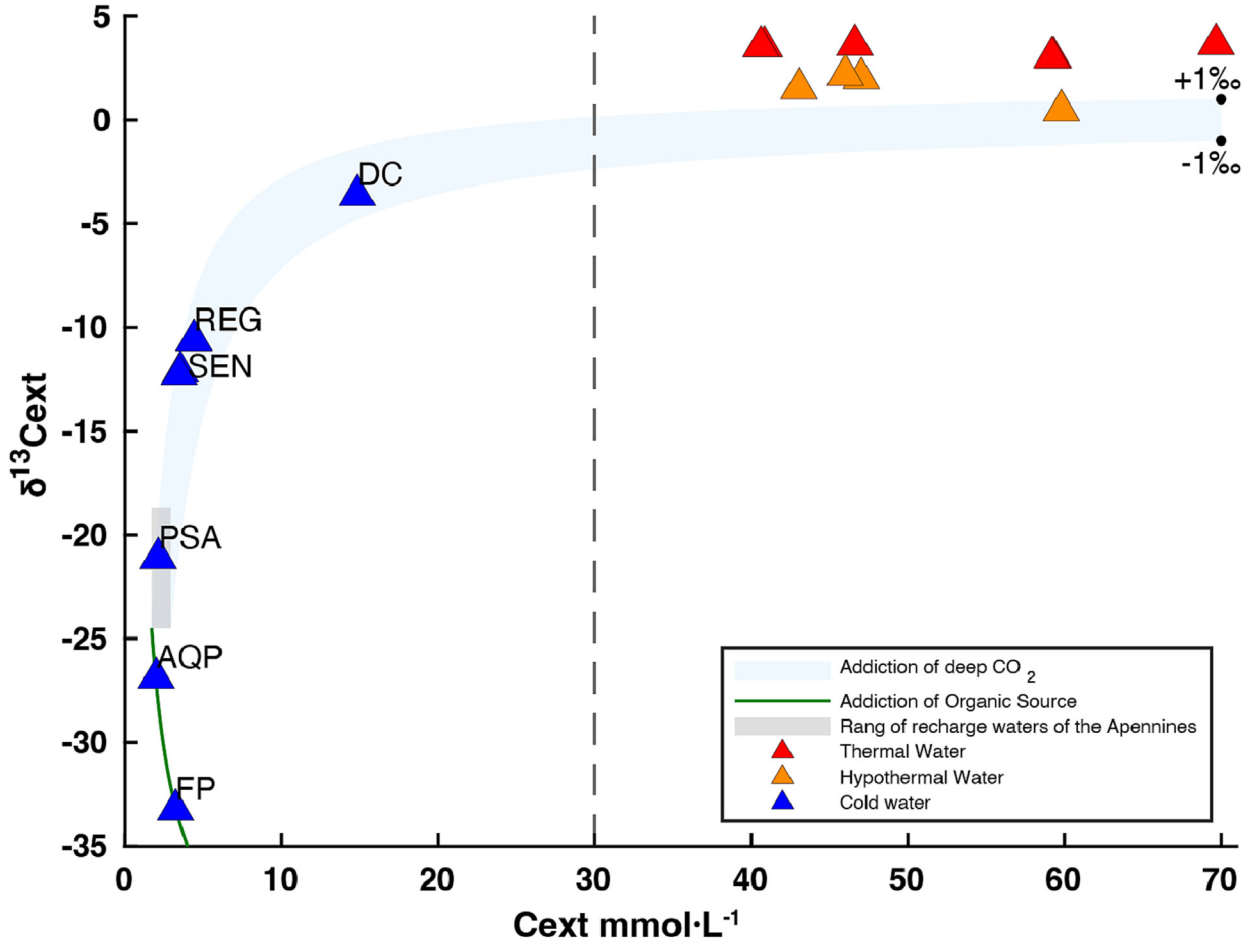

Fig. 5. Cext vs. δ^{13}Cext diagram. The theoretical field resulting from the addition of Cdeep with δ^{13}Cdeep ranging from −1 to +1 ‰ to infiltrating water with Cinf = 2.31 ± 0.61 mmol·L^{-1} and δ^{13}Cinf = −21.6 ± 2.9 ‰ is indicated in Frondini et al., 2019. The green line represents the theoretical mixing between the infiltrating water and an organic source. The dashed vertical line represents the Cext upper limit for the applicability of the no-sink assumption.

dissolution) has no impact on the CO_2 signature. However, in presence of carbon rich lithologies (as in the study area) the deep CO_2 interact with the carbon-rich lithology during its transfer through the crust and storage within the natural reservoirs, modifying its pristine carbon isotopic signature, before an additional interaction within more superficial water-rock systems.

In the study area, previous geophysical investigations (Improta et al., 2014) highlight the presence of dry deep CO_2 traps at depth between 7 and 13 km within the Triassic dolostones and anhydrites, the former a lithology containing carbon. Moreover, Improta et al., 2014, also highlight the presence of a shallower waters dominated reservoirs mainly composed of carbonate-dominated lithology at depth between 1 and 4 Km.

The investigation started discussing how the pristine carbon isotopic composition of CO_2 can be modified in the deep reservoirs, as a result of the CO_2-dolomite interaction and the subsequent water-rock interaction within the shallower reservoirs.

To study the CO_2-dolomite interaction, a dolomite sample with a density of $2.87{\cdot}10^3$ kg·m^{-3} (Schön, 2011) and a porosity up to of 0.1 % was considered. The density of CO_2 varies between 999.3 and 1042 kg·m^{-3}. Under these conditions, it is found that the mass of dolomite is up to thirty times greater than the mass of CO_2.

For the latter scenario, even with low residence times (i.e., short gas-rock interaction times), the result of the $\delta^{13}C_{CO_2(gas)}$ fractionation of CO_2 in equilibrium with dolomite can be considered to fit the equation.

$$\varepsilon_{CO_2\ -\ dolomite} = \delta^{13}C_{CO_2(gas)} - \delta^{13}C_{dolomite} \tag{5}$$

Using the thermal profiles provided by Boncio et al., 2007, the temperatures within the crust at the depth of the dry reservoir range from 190 °C (at a depth of 7 km) to 340 °C (at a depth of 13 km). Under these conditions, the value of $\varepsilon_{CO_2\ -\ dolomite}$ varies between −0.26 to +1.19 ‰, (Horita, 2014), −1.33 to +4.13 ‰, (Schauble et al., 2006) and + 2.39 to +4.27 ‰, (Deines, 2004).

By considering the signature of Apennine Triassic dolomite ($\delta^{13}C_{dolomite}$ = 3.45 ‰, mean value in (De Paola et al., 2011) and solving the Eq. (5) and solving for $\delta^{13}C_{CO2\ (gas)}$, an estimation is made for the deep reservoir in equilibrium with host rocks is made. The result indicates that the deep reservoir, regardless of its pristine origin (decarbonation or magma/mantle), is characterized by $\delta^{13}C_{CO2\ (deep)}$ values ranging from +2.12 to +7.72 ‰. This wide range of values partially overlap the range of −1/+1 ‰, calculated by using the mixing model (Section 4.2).

The CO_2 that has undergone equilibration with rocks in deep dry reservoirs subsequently migrates towards the surface, where it interacts with the rocks and water it encounters. In the following sections of this study, the interactions between CO_2, water, and salt waters in shallow crustal layers are modeled. This involves reconstructing the dynamics of CO_2-water/salt waters interactions, while also considering the effects of CO_2 degassing and calcite precipitation.

5.2. CO_2-water/salt waters interactions in shallow crustal layers

After having interacted with dolomite rocks within the natural reservoirs under the Apulian Platform, the deep CO_2 migrates upward through an intricate pattern of active faults, until reaching first the shallow water-saturated fluid reservoirs in the carbonate lithology and then the surface.

More in detail, the shallower CO_2 gas caps at a depth of 1–4 km are characterized by the presence of brines (Improta et al., 2014). To model the CO_2-rock-water phase interaction in the shallow crustal layers of the study area, two conditions were separately considered to represent possible scenarios at depth: 1) a low salinity water-saturated aquifer, and 2) a salt water-rich reservoir.

A carbonate-water system (an aquifer in carbonate rocks) in presence of CO_2 is well described by following equation (Mook, 2001):

$$\left(\frac{K_0K_1}{[H^+]} + 2\frac{K_0K_1K_2}{[H^+]^2}\right)P_{CO_2}^2 \left(\frac{K_w}{[H^+]} - [H^+]\right)P_{CO_2} + 2\frac{K_{cal}[H^+]^2}{K_0K_1K_2} = 0 \tag{6}$$

where the carbonate-water equilibrium constants are dependent on temperature, pH and P_{CO_2}. The combination of these parameters establishes the abundance of each carbon specie and can be given in terms of H_2CO_3, according to the following equations (Mook, 2001):

$$[H_2CO_3] = K_0P_{CO_2} \tag{7}$$

$$\left[HCO_3^-\right] = \frac{K_1}{[H^+]}[H_2CO_3] \tag{8}$$

$$\left[CO_3^{2-}\right] = \frac{K_1K_2}{[H^+]^2}[H_2CO_3] \tag{9}$$

where, the ionic product of water (K_w) comes from the equation by (Dickson and Riley, 1979), the molar solubility K_0 (mol·l^{-1}·atm^{-1}) is obtained by (Dickson et al., 2007), the first and second dissociation constants of carbonic acid (K_1 and K_2) are obtained by (Dickson and Millero, 1987), and the solubility constant of calcite is obtained by (Mucci, 1983).

The following isotope mass balance can be used to define the $\delta^{13}C$ values of TDIC and CO_2(aq) resulting from CO_2(gas) dissolution, assuming (i) that TDIC is entirely derived from CO_2(gas) dissolution and CO_2(aq) conversion, and (ii) that gaseous and dissolved carbon species achieve isotopic equilibrium:

$$\delta^{13}C_{TDIC} = \delta^{13}C_{CO_2} + \varepsilon_{TDIC\ -\ CO_2(gas)} \tag{10}$$

were $\varepsilon_{TDIC\ -\ CO_2(gas)}$ is obtained by summing up the fractionation factors between each dissolved carbon species (CO_{2aq}, HCO_3^-, CO_3^{2-}) and CO_2, weighted for their abundance with respect to total dissolved carbon, as follows (Capasso et al., 2005a; Grassa et al., 2006):

$$\varepsilon_{TDIC\ -\ CO_2(gas)} = \varepsilon_{HCO_3^-\ -\ CO_2(gas)}{\cdot}X_{HCO_3^-} + \varepsilon_{CO_2(d)\ -\ CO_2(gas)}{\cdot}X_{H_2CO_3} + \varepsilon_{CO_3^{2-}\ -\ CO_2(gas)}{\cdot}X_{CO_3^{2-}} \tag{11}$$

Where X represents the mole fraction, calculated using the Eqs. (7)–(9). The enrichment factors $\varepsilon_{HCO_3^-\ -\ CO_2(gas)}$ and $\varepsilon_{CO_2(d)\ -\ CO_2(gas)}$ are defined by Mook et al., 1974 for fresh water and by Myrttinen et al., 2015 for non-ideal solution such as a salt water (S = 35 ‰).

The values for $\delta^{13}C_{TDIC}$ resulting from the interaction between the previously calculated $\delta^{13}C_{CO_2\ (deep)}$ (+2.12 to +7.72 ‰, Section 5.1) and water with S = 0 ‰ or 35 ‰ can be calculated using Eqs. (10) and (11). By considering waters with a pH in the range of 5.3–5.6 and temperatures close to the highest recorded in the study area (49 °C in ERC-S22 site; Table 1), values of $\delta^{13}C_{TDIC}$ between +2.22 ‰ and + 7.82 ‰ were obtained for low salinity waters (S = 0 ‰), while values between +3.29 ‰ and + 8.89 ‰ were obtained for salt-type waters (S = 35 ‰). These values are in the range of thermal and hypothermal waters, but they markedly differ from the negative values measured in the cool water.

After conducting a thorough analysis of the dynamics between deep reservoir gases and shallower aquifers located at depths ranging from 1 to 4 km, it becomes evident that further examination of the degassing or precipitation processes is necessary to better constrain the isotopic signature of initial conditions.

5.3. Aquifer CO_2-degassing

To evaluate the potential contribution of the CO_2 degassing process in modifying the TDIC and $\delta^{13}C_{TDIC}$ values in thermal and hypothermal waters, the effects of $\delta^{13}C$ of TDIC $\left(\delta^{13}C_{TDIC}\right)$ and the extracted CO_2 $\left(\delta C_{CO_2\ (g)\ 13}\right)$ were modeled using a Rayleigh distillation process (Hoefs, 2009):

$$\delta^{13}C_{TDIC(res)} = \left(\delta^{13}C_{TDIC(init)} + 10^3\right){\cdot}F^{1/\alpha_{TDIC\ -\ CO_2(g)}\ -\ 1} - 10^3 \tag{12}$$

Where $\delta^{13}C_{TDIC(init)}$ is the initial isotopic composition of the TDIC in the hydrothermal fluid, $\delta^{13}C_{TDIC(res)}$ is the isotopic composition of the residual

TDIC after CO_2 degassing, F is the fraction of CO_2 remaining after degassing and $\alpha_{TDIC\ -\ CO_2(g)}$ is derived from Eq. (11) as follows:

$$\alpha_{TDIC\ -\ CO_2(g)} = \frac{\varepsilon_{TDIC\ -\ CO_2(g)}}{10^3} + 1 \quad (13)$$

Due to the differing fractionation factors between dissolved carbon species and CO_2, the fractionation factor $\alpha_{TDIC\ -\ CO_2(g)}$ is pH-dependent (greater for higher pH values).

The initial conditions of the aquifer prior to the degassing are currently unknown. To determine the optimal starting point for the degassing process, Eqs. (6)–(13) were utilized, and variations in the values of P_{CO_2} and $\delta^{13}C_{CO_{2\ (deep)}}$ were systematically applied, resulting in different TDIC and $\delta^{13}C_{TDIC}$ values for the aquifer. The theoretical curves generated from Eq. (12) were then compared with measured values from thermal sites. The coefficient of determination (R2) is employed to assess the correspondence between the model and the measured values, utilizing the "distance-2-curve" (D'Errico, 2023) and "rsquare" (Hebeler, 2023).

Therefore, for a salinity of 0 ‰, the best fit (R^2 of 0.94) is obtained with an initial TDIC amount of 80 mmol·L^{-1} and a $\delta^{13}C_{TDIC}$ value of 3.30 ‰. In turn, these initial conditions correspond to a $\delta^{13}C_{CO_{2\ (deep)}}$ =3.2 ‰ and $\varepsilon_{TDIC\ -\ CO_2(g)}$ = 0.10 ‰, as calculated by Eq. (11) (Fig. 6a).

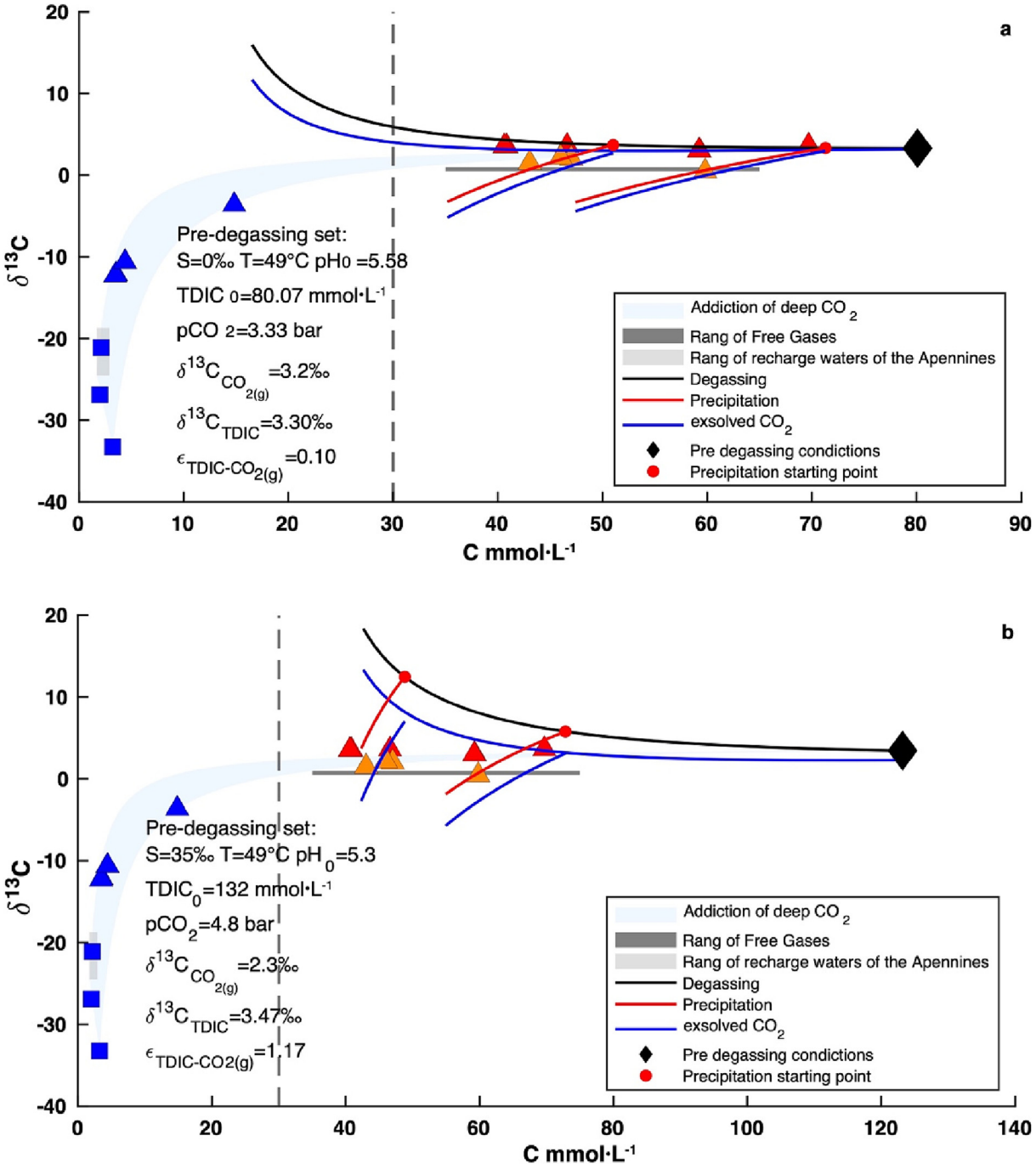

Fig. 6. Carbon content vs. $\delta^{13}C$ diagram in salt water-gas-rocks interaction. The theoretical field resulting from the addition of Cdeep with $\delta^{13}C_{TDIC}$ = +3.30 ‰ for low salinity water (a) and 3.47 ‰ for salt water (b), to infiltrating water is indicated in light blue field. The dashed vertical line represents the Cext upper limit for the applicability of the no-sink assumption. The black line represents the evolution of $\delta^{13}C_{TDIC}$ after degassing, while the red line represents the evolution after precipitations. The blue line indicates the associated $\delta^{13}C_{CO_2(g\ -\ res)}$.

In the same way, for a salinity of 35 ‰, the theoretical curve does not agree with the measured values and the best fit ($R^2 = 0.3$) is obtained with an initial TDIC value of 132 mmol·L^{-1} and a $\delta^{13}C_{CO_2\ (deep)}$ value of 2.3, resulting in a $\delta^{13}C_{TDIC}$ value of 3.47 ‰, as seen in Fig. 6b. These initial conditions correspond to a $\delta^{13}C_{CO_2\ (deep)}$ value of 2.12, and $\varepsilon_{TDIC\ -\ CO_2(g)} = 1.17$ ‰.

In any case, the obtained $\delta^{13}C_{CO_2\ (deep)}$ values for S = 0 ‰ and S = 35 ‰ are consistent with the hypothesized gas-dolomite interaction a temperature range of 224–184 °C (corresponding to a depth range of 8.30–7.10 km).

5.4. Calcite precipitation effect

As debated above, the measured $\delta^{13}C_{TDIC}$ values for samples with TDIC levels higher than 30 mmol·L^{-1} cannot be solely accounted for by degassing. Thus, the possibility of isotopic fractionation caused by calcite precipitation during water circulation is taken into account to gain a comprehensive understanding of the carbon amount and isotopic composition in the water emerging in the study area.

Under open-system conditions calcite precipitation can be described as a Rayleigh-type fractionation process, as follows:

$$\delta^{13}C_{TDIC(res)} = \left(\delta^{13}C_{TDIC(init)} + 10^3\right)\cdot F'^{\alpha_{calcite\ -\ TDIC}\ -\ 1} - 10^3 \quad (14)$$

where F' is the fraction of residual TDIC and $\alpha_{calcite\ -\ TDIC}$ is the isotopic fractionation factor between calcite and TDIC computed, as follows (Venturi et al., 2017):

$$\alpha_{calcite\ -\ TDIC} = \left[\varepsilon_{calcite\ -\ CO_2(g)} - \left(X_{H_2CO_3}\cdot\varepsilon_{CO_2(aq)\ -\ CO_2(g)}\right) + \left(X_{HCO_3^-}\cdot\varepsilon_{HCO_3^-\ -\ CO_2(g)}\right)\right]\cdot 10^{-3} + 1 \quad (15)$$

The $\varepsilon_{CO_2(aq)\ -\ CO_2(g)}$ value is calculated as in Eq. (2), whereas $\varepsilon_{calcite\ -\ CO_2(g)}$ were calculated using the equations proposed by Deines et al. (1974), as follows:

$$\varepsilon_{calcite\ -\ CO_2(g)} = \frac{1194000}{T^2} - 3.63 \quad (16)$$

By the Eq. (14) and selecting a suitable starting point from the degassing curve, the calcite precipitation curves (red lines in Fig. 6a) were calculated. The same approach is used for a saltwater-dominated system (red lines in Fig. 6b). From Figs.6a and 6b it is possible to observe that the measured $\delta^{13}C_{TDIC}$ of both the salty thermal and hypothermal water samples is likely the result of calcite precipitation considering an initial amount of carbon dissolved in the water of about 130 mmol·L^{-1}.

5.5. Free gases interpretation

In order to fully understand the fate of deep-CO_2 that migrates to the surface and integrate in a model also the processes that control the chemistry of the free gases outgassing in the study area, The relationship between the dissolved carbon in the waters and the outgassing CO_2 is being reconstructed by modeling the fraction of CO_2 exsolved from the aquifer using the Rayleigh fractionation process (Hoefs, 2009):

$$\delta^{13}C_{CO_2(g\ -\ res)} = \alpha_{TDIC\ -\ CO_2(g)}\cdot\left(\delta^{13}C_{TDIC(init)} + 10^{+3}\right)\cdot F'^{\alpha_{TDIC\ -\ CO_2(g)}\ -\ 1} - 10^{+3} \quad (17)$$

where the $\alpha_{TDIC\ -\ CO_2(g)}$ is calculated following the Eq. (13) for S = 0 ‰ and S = 35 ‰.

To investigate the possibility that the $\delta^{13}C_{CO_2}$ values observed in free gas occurrences in the area are a result of CO_2 degassing and concurrent calcite precipitation in the aquifer, the values of $\delta^{13}C_{CO_2}$ of residual $CO_{2(gas)}$ $\left(\delta^{13}C_{CO_2\ (res)}\right)$ were computed as a function of the residual fraction F′ using Eq. (17). It is found that the $\delta^{13}C_{CO_2\ (res)}$ values from thermal and hypothermal water align with those observed on the surface ($\delta^{13}C_{CO_2}$ = 0.7 ‰ for SST and $\delta^{13}C_{CO_2}$ = 0.86‰ for OV1). These results highlight that the free gases locally emerging at the surface escape from the groundwaters in shallow crustal layers.

5.6. Output of deeply derived CO_2

The Contursi basin, is characterized by two types of gaseous manifestations, including dissolved and free gases. Actually, both of them collectively contribute to the CO_2 budget emitted into the atmosphere in this active tectonic region. To quantify the output of deeply derived CO_2, carbon mass balance calculations were conducted on the studied aquifers to estimate the free gas flux. These calculations offer valuable insights into the budget of CO_2 released from deep within the Earth's crust and its impact on the local geochemical environment.

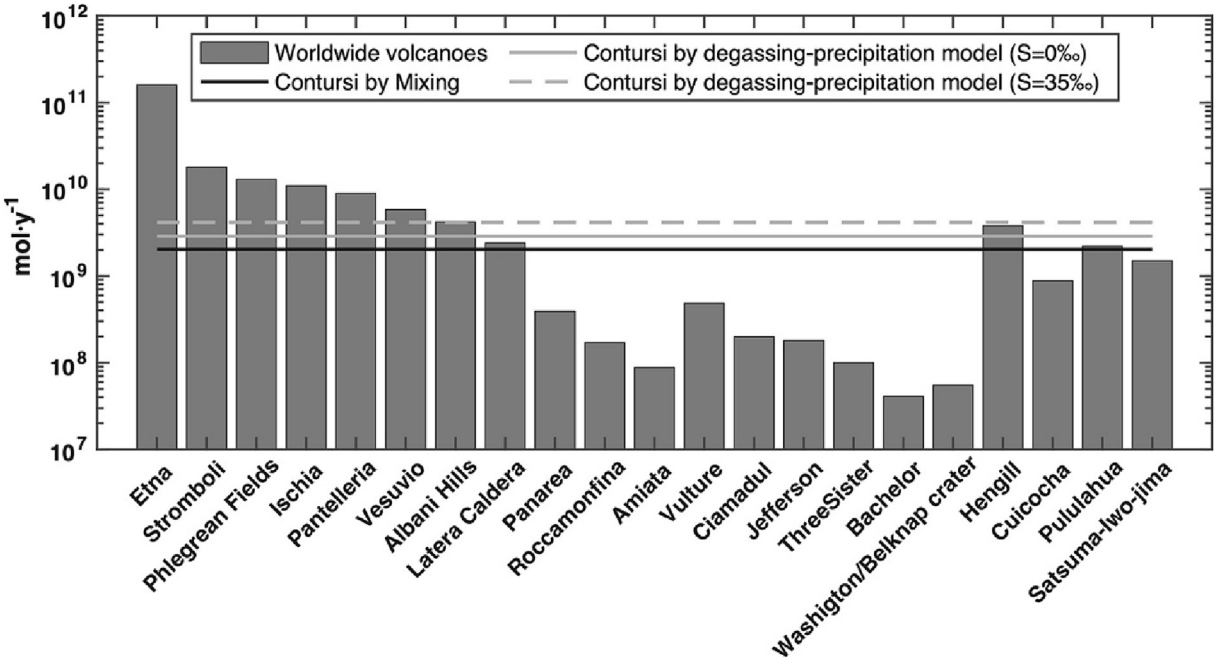

Fig. 7. CO_2 Output (free plus dissolved) in mol·y^{-1}. Assumptions that exclude secondary processes (black full line) can underestimate CO_2 outputs by up to twice as much. The total budget of mantle-derived CO_2 from worldwide volcanoes is reported for comparison (Caracausi and Paternoster, 2015).

According to the mixing model (Section 4.2, Chiodini et al., 2000) the deep CO_2 output computed by using the product between the Cdeep and the water flow rate (Q, in $L{\cdot}s^{-1}$) for each site is between 3.7 10^5 $mol{\cdot}y^{-1}$ and 6.4 10^8 $mol{\cdot}y^{-1}$ (Table 4 and Fig. 6).

However, it is observed that the thermal and hypothermal waters collected are characterized by a CO_2-rich groundwater (ranging from 80 to 130 $mmol{\cdot}L^{-1}$ for S = 0 ‰ and S = 35 ‰ water, respectively) which undergoes degassing and calcite precipitation (refer to Sections 5.3 and 5.4; Fig. 5). Furthermore, the cold waters result from a mixing between the CO_2-rich groundwater and an infiltration wate.

Once all the terms of the carbon budget are determined, the total output of deep-CO_2 associated to the cold water is $Q_{CO_2\text{-deep,cold}}$ = 4.2 10^{+8} $mol{\cdot}y^{-1}$, with the hypothermal water is $Q_{CO_2\text{-deep,hypot}}$ = 8.91 10^{+8} $mol{\cdot}y^{-1}$ and with the thermal water is $Q_{CO_2\text{-deep,hypot}}$ = 1.86 10^{+8} $mol{\cdot}y^{-1}$. Therefore, the total CO_2 budget (as sum of the three components) corresponds to $Q_{CO_2\text{-deep,dis}}$ = 1.50·10^{+9} $mol{\cdot}y^{-1}$.

Considering free sources are also taken into consideration, such as the one associated with SST (which is the only source for which a flux value is available in the existing literature), $Q_{CO2\text{-deep,free}}$ is equal to 4.82·10^{+8} $mol{\cdot}y^{-1}$ (Italiano et al., 2000), and the total output in the area becomes $Q_{CO2\text{-tot}}$ = 1.98·10^{+9} $mol{\cdot}y^{-1}$.

The latter value, even if it might be underestimated due to the partial knowledge of data on flow rates and the influence of secondary processes, is comparable with total budget of mantle-derived CO_2 in active and quiescent volcanic systems (see Fig. 7). Considering degassing and precipitation processes the total output become 1.98·10^{+9} $mol{\cdot}y^{-1}$ if S = 0 ‰ and 4.08·10^{+9} $mol{\cdot}y^{-1}$ if S = 35 ‰, that is 40 % and twice the previous value respectively.

As a result, the utilization of an alternative geochemical model, as performed in this study, illustrates the potential for actual gas outputs in the Irpinia region to be significantly greater than those calculated utilizing simplified models. It is important to note that these estimates may fluctuate if secondary processes occur during the movement of fluids towards the surface.

6. Conclusions

The main aim of this study is to investigate the processes of gas-water-rock interaction that governs the chemical composition of crustal fluids within the Irpinia zone (Southern Apennines, Italy), through the analysis of He—C systematics and the interplay between mantle/magmatic and crustal fluids.

From 2300 earthquakes that occurred in the Irpinia fault zone between 2008 and 2019, the data revealed that seismicity is mainly localized in two layers: shallow and low magnitude earthquakes (2 km to 4 km depth, up to M 3.3) associated with shallow-water carbonates reservoir, and deeper and more intense earthquakes (6 km to 9 km depth, up to magnitude M 4.4) coincident with a dry pressurized reservoir.

A regional degassing of mantle-derived He is confirmed. The variability of the $C/^4He$ elemental ratio, despite the overall steady $^3He/^4He$ ratio in the samples, can be attributed to the different geochemical behaviour of He and CO_2, suggesting the occurrence of secondary processes such as CO_2 loss (degassing/calcite precipitation) and the addition of crustal CO_2 and ^4He.

Gas-rock interaction occurring in the dry reservoirs at depths between 7 and 8.6 km can modify the isotopic signature of CO_2 stored into the deep dolomitic reservoirs, potentially hindering its original carbon isotopic signature. Furthermore, the interaction of deep CO_2 with water or brine can further changes its isotopic signature. In fact, through mixing (for cold water) and secondary gas-water interaction processes such as precipitation and degassing, CO_2 acquires the final isotopic signature of the fluids typical of the studied area.

Understanding the processes of gas-water-rock interaction at depth is a crucial factor for unveiling the relationship between geochemical changes accompanying large earthquakes and the degassing on a large scale, and to obtain a better evaluation of natural CO_2 emissions into the atmosphere.

CRediT authorship contribution statement

Dario Buttitta: Conceptualization, Methodology, Investigation, Formal analysis, Software, Data curation, Writing – original draft. **Giorgio Capasso:** Methodology, Supervision, Writing – review & editing. **Michele Paternoster:** Methodology, Investigation, Validation, Supervision. **Marino Domenico Barberio:** Methodology, Investigation. **Francesca Gori:** Methodology, Investigation. **Marco Petitta:** Methodology, Investigation, Validation, Supervision. **Matteo Picozzi:** Methodology, Investigation, Validation, Supervision. **Antonio Caracausi:** Conceptualization, Methodology, Supervision, Project administration, Writing – original draft, Writing – review & editing.

Data availability

All data used in this work can be found in Gori et al. 2023 "Hydrogeochemical multi-component approach to assess fluids upwelling and mixing in shallow carbonate-evaporitic aquifers (Contursi area)"

Declaration of competing interest

The authors declare that they have no known competing financial interests or personal relationships that could have appeared to influence the work reported in this paper.

Acknowledgements

This research was carried out in the frame of the national project PRIN-FLUIDS (Grant Number 20174X3P29_005) and the national PON GRINT (Geoscience Research INfrastructure in iTaly) CCI:2014IT16M2OP005. Antonio Caracausi appreciates support by the “Ramón y Cajal” research program (RYC2021-033270-I; MCIN/AEI/10.13039/501100011033 - EU “NextGenerationEU/PRTR”).

References

Aggarwal, P.K., Matsumoto, T., Sturchio, N.C., Chang, H.K., Gastmans, D., Araguas-Araguas, L.J., Jiang, W., Lu, Z.T., Mueller, P., Yokochi, R., Purtschert, R., Torgersen, T., 2015. Continental degassing of ^4He by surficial discharge of deep groundwater. Nat. Geosci. 8, 35–39. https://doi.org/10.1038/ngeo2302.

Amoroso, O., Ascione, A., Mazzoli, S., Virieux, J., Zollo, A., 2014. Seismic imaging of a fluid storage in the actively extending Apennine mountain belt, southern Italy. Geophys. Res. Lett. 41, 3802–3809. https://doi.org/10.1002/2014gl060070.

Amoroso, O., Russo, G., De Landro, G., Zollo, A., Garambois, S., Mazzoli, S., Parente, M., Virieux, J., 2017. From velocity and attenuation tomography to rock physical modeling: inferences on fluid-driven earthquake processes at the Irpinia fault system in southern Italy. Geophys. Res. Lett. 44, 6752–6760. https://doi.org/10.1002/2016gl072346.

Ascione, A., Mazzoli, S., Petrosino, P., Valente, E., 2013. A decoupled kinematic model for active normal faults: insights from the 1980, MS = 6.9 Irpinia earthquake, southern Italy. GSA Bull. 125, 1239–1259. https://doi.org/10.1130/B30814.1.

Ballentine, C.J., Sherwood Lollar, B., 2002. Regional groundwater focusing of nitrogen and noble gases into the Hugoton-panhandle giant gas field, USA. Geochim. Cosmochim. Acta 66, 2483–2497. https://doi.org/10.1016/S0016-7037(02)00850-5.

Barberio, M.D., Barbieri, M., Billi, A., Doglioni, C., Petitta, M., 2017. Hydrogeochemical changes before and during the 2016 Amatrice-Norcia seismic sequence (Central Italy). Sci. Rep. 7, 11735. https://doi.org/10.1038/s41598-017-11990-8.

Boncio, P., Mancini, T., Lavecchia, G., Selvaggi, G., 2007. Seismotectonics of strike–slip earthquakes within the deep crust of southern Italy: geometry, kinematics, stress field and crustal rheology of the Potenza 1990–1991 seismic sequences (Mmax 5.7). Tectonophysics 445, 281–300. https://doi.org/10.1016/j.tecto.2007.08.016.

Bragagni, A., Mastroianni, F., Münker, C., Conticelli, S., Avanzinelli, R., 2022. A carbon-rich lithospheric mantle as a source for the large CO_2 emissions of Etna volcano (Italy). Geology 50, 486–490. https://doi.org/10.1130/G49510.1.

Buttitta, D., Caracausi, A., Chiaraluce, L., Favara, R., Gasparo Morticelli, M., Sulli, A., 2020. Continental degassing of helium in an active tectonic setting (northern Italy): the role of seismicity. Sci. Rep. 10, 162. https://doi.org/10.1038/s41598-019-55678-7.

Capasso, G., Inguaggiato, S., 1998. A simple method for the determination of dissolved gases in natural waters. An application to thermal waters from Vulcano Island. Appl. Geochem. 13, 631–642. https://doi.org/10.1016/S0883-2927(97)00109-1.

Capasso, G., Carapezza, M.L., Federico, C., Inguaggiato, S., Rizzo, A., 2005a. Geochemical monitoring of the 2002–2003 eruption at Stromboli volcano (Italy): precursory changes in the carbon and helium isotopic composition of fumarole gases and thermal waters. Bull. Volcanol. 68, 118–134. https://doi.org/10.1007/s00445-005-0427-5.

Capasso, G., Favara, R., Grassa, F., Inguaggiato, S., Longo, L., 2005b. On-line technique for preparingand measuring stable carbon isotopeof total dissolved inorganic carbonin water samples ($d^{13}C_{TDIC}$). Ann. Geophys. 48. https://doi.org/10.4401/ag-3190.

Caracausi, A., Paternoster, M., 2015. Radiogenic helium degassing and rock fracturing: a case study of the southern Apennines active tectonic region. J. Geophys. Res. Solid Earth 120, 2200–2211. https://doi.org/10.1002/2014JB011462.Received.

Caracausi, A., Sulli, A., 2019. Outgassing of mantle volatiles in compressional tectonic regime away from volcanism: the role of continental delamination. Geochem. Geophys. Geosyst. 20, 2007–2020. https://doi.org/10.1029/2018GC008046.

Caracausi, A., Favara, R., Italiano, F., Nuccio, P.M., Paonita, A., Rizzo, A., 2005. Active geodynamics of the Central Mediterranean Sea: tensional tectonic evidences in western Sicily from mantle-derived helium. Geophys. Res. Lett. 32, 1–5. https://doi.org/10.1029/2004GL021608.

Caracausi, A., Martelli, M., Nuccio, P.M., Paternoster, M., Stuart, F.M., 2013. Active degassing of mantle-derived fluid: a geochemical study along the vulture line, southern Apennines (Italy). J. Volcanol. Geotherm. Res. 253, 65–74. https://doi.org/10.1016/j.jvolgeores.2012.12.005.

Caracausi, A., Buttitta, D., Picozzi, M., Paternoster, M., Stabile, T.A., 2022. Earthquakes control the impulsive nature of crustal helium degassing to the atmosphere. Communications Earth & Environment 3, 1–8. https://doi.org/10.1038/s43247-022-00549-9.

Carnevale, G., Caracausi, A., Rotolo, S.G., Paternoster, M., Zanon, V., 2022. New inferences on magma dynamics in melilitite-carbonatite volcanoes: the case study of mt. vulture (southern Italy). Geophys. Res. Lett. 49. https://doi.org/10.1029/2022gl099075.

Cavazza, W., Roure, F.M., Spakman, W., Stampfli, G.M., Ziegler, P.A., 2012. The TRANSMED Atlas. The Mediterranean Region from Crust to Mantle: Geological and Geophysical Framework of the Mediterranean and the Surrounding Areas. Springer Science & Business Media https://doi.org/10.1007/978-3-642-18919-7.

Chiodini, G., Frondini, F., Kerrick, D.M., Rogie, J., Parello, F., Peruzzi, L., Zanzari, A.R., 1999. Quantification of deep CO_2 fluxes from Central Italy. Examples of carbon balance for regional aquifers and of soil diffuse degassing. Chem. Geol. 159, 205–222. https://doi.org/10.1016/S0009-2541(99)00030-3.

Chiodini, G., Frondini, F., Cardellini, C., Parello, F., Peruzzi, L., 2000. Rate of diffuse carbon dioxide earth degassing estimated from carbon balance of regional aquifers: the case of central Apennine, Italy. J. Geophys. Res. 105, 8423–8434. https://doi.org/10.1029/1999JB900355.

Chiodini, G., Cardellini, C., Amato, A., Boschi, E., Caliro, S., Frondini, F., Ventura, G., 2004. Carbon dioxide earth degassing and seismogenesis in central and southern Italy. Geophys. Res. Lett. 31. https://doi.org/10.1029/2004GL019480.

Chiodini, G., Granieri, D., Avino, R., Caliro, S., Costa, A., Minopoli, C., Vilardo, G., 2010. Non-volcanic CO_2 earth degassing: case of Mefite d'Ansanto (southern Apennines), Italy. Geophys. Res. Lett. 37. https://doi.org/10.1029/2010gl042858.

Chiodini, G., Caliro, S., Cardellini, C., Frondini, F., Inguaggiato, S., Matteucci, F., 2011. Geochemical evidence for and characterization of CO_2 rich gas sources in the epicentral area of the Abruzzo 2009 earthquakes. Earth Planet. Sci. Lett. 304, 389–398. https://doi.org/10.1016/j.epsl.2011.02.016.

Chiodini, G., Cardellini, C., Luccio, F.D., Selva, J., Frondini, F., Caliro, S., Rosiello, A., Beddini, G., Ventura, G., 2020. Correlation between tectonic CO_2 earth degassing and seismicity is revealed by a 10-year record in the Apennines, Italy. Science. Advances 6, eabc2938. https://doi.org/10.1126/sciadv.abc2938.

Cocco, M., Pacor, F., 1993. The rupture process of the 1980 Irpinia, Italy, earthquake from the inversion of strong motion waveforms. Tectonophysics 218, 157–177. https://doi.org/10.1016/0040-1951(93)90266-M.

Coppola, M., Correale, A., Barberio, M.D., Billi, A., Cavallo, A., Fondriest, M., Nazzari, M., Paonita, A., Romano, C., Stagno, V., Viti, C., Vona, A., 2021. Meso- to nano-scale evidence of fluid-assisted co-seismic slip along the normal Mt. Morrone fault, Italy: implications for earthquake hydrogeochemical precursors. Earth Planet. Sci. Lett. 568, 117010. https://doi.org/10.1016/j.epsl.2021.117010.

Curzi, M., Bernasconi, S.M., Billi, A., Boschi, C., Aldega, L., Franchini, S., Albert, R., Gerdes, A., Barberio, M.D., Looser, N., Carminati, E., 2021. U-Pb age of the 2016 Amatrice earthquake causative fault (Mt. Gorzano, Italy) and paleo-fluid circulation during seismic cycles inferred from inter- and co-seismic calcite. Tectonophysics 819, 229076. https://doi.org/10.1016/j.tecto.2021.229076.

Curzi, M., Cipriani, A., Aldega, L., Billi, A., Carminati, E., Van der Lelij, R., Vignaroli, G., Viola, G., 2023. Architecture and permeability structure of the Sibillini Mts. Thrust and influence upon recent, extension-related seismicity in the central Apennines (Italy) through fault-valve behavior. GSA. Bulletin. https://doi.org/10.1130/B36616.1.

D'Agostino, N., Silverii, F., Amoroso, O., Convertito, V., Fiorillo, F., Ventafridda, G., Zollo, A., 2018. Crustal deformation and seismicity modulated by groundwater recharge of karst aquifers. Geophys. Res. Lett. 45, 12,253–12,262. https://doi.org/10.1029/2018gl079794.

De Landro, G., Amoroso, O., Russo, G., D'Agostino, N., Esposito, R., Emolo, A., Zollo, A., 2022. Author correction: decade-long monitoring of seismic velocity changes at the Irpinia fault system (southern Italy) reveals pore pressure pulsations. Sci. Rep. 12, 16039. https://doi.org/10.1038/s41598-022-20912-2.

De Paola, N., Hirose, T., Mitchell, T., Di Toro, G., Viti, C., Shimamoto, T., 2011. Fault lubrication and earthquake propagation in thermally unstable rocks. Geology 39, 35–38. https://doi.org/10.1130/G31398.1.

Deines, P., 2004. Carbon isotope effects in carbonate systems. Geochim. Cosmochim. Acta 68, 2659–2679. https://doi.org/10.1016/j.gca.2003.12.002.

Deines, P., Langmuir, D., Harmon, R.S., 1974. Stable carbon isotope ratios and the existence of a gas phase in the evolution of carbonate ground waters. Geochim. Cosmochim. Acta 38, 1147–1164. https://doi.org/10.1016/0016-7037(74)90010-6.

D'Errico, John. 2023. Distance2curve - file exchange - MATLAB CentralFile exchange - MATLAB central (version 1.1.0.0). MATLAB central file exchange. https://it.mathworks.com/matlabcentral/fileexchange/34869-distance2curve.

Dickson, A.G., Millero, F.J., 1987. A comparison of the equilibrium constants for the dissociation of carbonic acid in seawater media. Deep Sea Res. A 34, 1733–1743. https://doi.org/10.1016/0198-0149(87)90021-5.

Dickson, A.G., Riley, J.P., 1979. The estimation of acid dissociation constants in seawater media from potentionmetric titrations with strong base. I. the ionic product of water — kw. Mar. Chem. 7, 89–99. https://doi.org/10.1016/0304-4203(79)90001-x.

Dickson, Andrew Gilmore, Sabine, Christopher L., Christian, James Robert, 2007. Guide to Best Practices for Ocean CO_2 Measurements. Edited by PICES Special Publication and IOCCP Report. North Pacific Marine Science Organization. Available to. https://www.ncei.noaa.gov/access/ocean-carbon-acidification-data-system/oceans/Handbook_2007.html.

Festa, G., Adinolfi, G.M., Caruso, A., Colombelli, S., De Landro, G., Elia, L., Emolo, A., Picozzi, M., Scala, A., Carotenuto, F., Gammaldi, S., Iaccarino, A.G., Nazeri, S., Riccio, R., Russo, G., Tarantino, S., Zollo, A., 2021. Insights into mechanical properties of the 1980 Irpinia fault system from the analysis of a seismic sequence. Geosci. J. 11, 28. https://doi.org/10.3390/geosciences11010028.

Frondini, F., Cardellini, C., Caliro, S., Beddini, G., Rosiello, A., Chiodini, G., 2019. Measuring and interpreting CO2 fluxes at regional scale: the case of the Apennines, Italy. J. Geol. Soc. London 176, 408–416. https://doi.org/10.1144/jgs2017-169.

Gautheron, C., Moreira, M., Allègre, C., 2005. He, ne and Ar composition of the European lithospheric mantle. Chem. Geol. 217, 97–112. https://doi.org/10.1016/j.chemgeo.2004.12.009.

Ghisetti, F., Vezzani, L., 2002. Normal faulting, transcrustal permeability and seismogenesis in the Apennines (Italy). Tectonophysics 348, 155–168. https://doi.org/10.1016/S0040-1951(01)00254-2.

Gilfillan, S.M.V., Lollar, B.S., Holland, G., Blagburn, D., Stevens, S., Schoell, M., Cassidy, M., Ding, Z., Zhou, Z., Lacrampe-Couloume, G., Ballentine, C.J., 2009. Solubility trapping in formation water as dominant CO_2 sink in natural gas fields. Nature 458, 614–618. https://doi.org/10.1038/nature07852.

Gori, F., Paternoster, M., Barbieri, M., Buttitta, D., Caracausi, A., Parente, F., Sulli, A., Petitta, M., 2023. Hydrogeochemical multi-component approach to assess fluids upwelling and mixing in shallow carbonate-evaporitic aquifers (Contursi area, southern Apennines, Italy). J. Hydrol. 618, 129258. https://doi.org/10.1016/j.jhydrol.2023.129258.

Grassa, F., Capasso, G., Favara, R., Inguaggiato, S., 2006. Chemical and isotopic composition of waters and dissolved gases in some thermal springs of Sicily and adjacent Volcanic Islands, Italy. Pure Appl. Geophys. 163, 781–807. https://doi.org/10.1007/s00024-006-0043-0.

Groppo, C., Rolfo, F., Frezzotti, M.L., 2022. CO_2 outgassing during collisional orogeny is facilitated by the generation of immiscible fluids. Communications Earth & Environment 3, 1–11. https://doi.org/10.1038/s43247-022-00340-w.

Halford, D.T., Karolytė, R., Barry, P.H., Whyte, C.J., Darrah, T.H., Cuzella, J.J., Sonnenberg, S.A., Ballentine, C.J., 2022. High helium reservoirs in the four corners area of the Colorado plateau, USA. Chem. Geol. 596, 120790. https://doi.org/10.1016/j.chemgeo.2022.120790.

Hebeler, F., 2023. rsquare.

Hoefs, J., 2009. Stable Isotope Geochemistry. 6th ed. Springer Science & Business Media, Berlin, Germany https://doi.org/10.1007/978-3-540-70708-0.

Holland, G., Gilfillan, S., 2012. Application of noble gases to the viability of CO2 storage. The Noble Gases as Geochemical Tracers, pp. 1–391 https://doi.org/10.1007/978-3-642-28836-4.

Horita, J., 2014. Oxygen and carbon isotope fractionation in the system dolomite–water–CO2 to elevated temperatures. Geochim. Cosmochim. Acta 129, 111–124. https://doi.org/10.1016/j.gca.2013.12.027.

Improta, L., De Gori, P., Chiarabba, C., 2014. New insights into crustal structure, Cenozoic magmatism, CO_2 degassing, and seismogenesis in the southern Apennines and Irpinia region from local earthquake tomography: seismic tomography of Apennines. J. Geophys. Res. Solid Earth 119, 8283–8311. https://doi.org/10.1002/2013JB010890.

Italiano, F., Martelli, M., Martinelli, G., Nuccio, P.M., 2000. Geochemical evidence of melt intrusions along lithospheric faults of the southern Apennines, Italy: geodynamic and seismogenic implications. J. Geophys. Res. Solid Earth 105, 13569–13578. https://doi.org/10.1029/2000jb900047.

Italiano, F., Martinelli, G., Nuccio, P.M., 2001. Anomalies of mantle-derived helium during the 1997-1998 seismic swarm of Umbria-Marche, Italy. Geophys. Res. Lett. 28, 839–842. https://doi.org/10.1029/2000GL012059.

Italiano, F., Caracausi, A., Favara, R., Innocenzi, P., Martinelli, G., 2005. Geochemical monitoring of cold waters during seismicity: implications for earthquake-induced modification in shallow aquifers. TAO 16, 709–729.

Italiano, F., Martinelli, G., Bonfanti, P., Caracausi, A., 2009. Long-term (1997-2007) geochemical monitoring of gases from the Umbria-Marche region. Tectonophysics 476, 282–296. https://doi.org/10.1016/j.tecto.2009.02.040.

Karolytė, R., Johnson, G., Györe, D., Serno, S., Flude, S., Stuart, F.M., Chivas, A.R., Boyce, A., Gilfillan, S.M.V., 2019. Tracing the migration of mantle CO_2 in gas fields and mineral water springs in south-East Australia using noble gas and stable isotopes. Geochim. Cosmochim. Acta 259, 109–128. https://doi.org/10.1016/j.gca.2019.06.002.

Kipfer, R., Aeschbach-Hertig, W., Peeters, F., Stute, M., 2002. Noble gases in lakes and ground waters. Rev. Mineral. Geochem. 47, 615–700. https://doi.org/10.2138/rmg.2002.47.14.

Klein, F., Goldsby, D.L., Lin, J., Andreani, M., 2022. Carbonation of serpentinite in creeping faults of California. Geophys. Res. Lett. 49. https://doi.org/10.1029/2022gl099185.

Krishnamurthy, P.G., DiCarlo, D., Meckel, T., 2022. Geologic heterogeneity controls on trapping and migration of CO_2. Geophys. Res. Lett. 49. https://doi.org/10.1029/2022gl099104.

Mabry, J., Lan, T., Burnard, P., Bernard, M., 2013. High-precision helium isotope measurements in air. J. Anal. At. Spectrom. 28, 1903–1910. https://doi.org/10.1039/c3ja50155h.

Marchesini, B., Carminati, E., Aldega, L., Mirabella, F., Petrelli, M., Caracausi, A., Barchi, M.R., 2022. Chemical interaction driven by deep fluids in the damage zone of a seismogenic carbonate fault. J. Struct. Geol. 161, 104668. https://doi.org/10.1016/j.jsg.2022.104668.

Marty, B., Almayrac, M., Barry, P.H., Bekaert, D.V., Broadley, M.W., Byrne, D.J., Ballentine, C.J., Caracausi, A., 2020. An evaluation of the C/N ratio of the mantle from natural CO_2-rich gas analysis: geochemical and cosmochemical implications. Earth Planet. Sci. Lett. 551, 116574. https://doi.org/10.1016/j.epsl.2020.116574.

Miller, S.A., Collettini, C., Chiaraluce, L., Cocco, M., Barchi, M., Kaus, B.J.P., 2004. Aftershocks driven by a high-pressure CO_2 source at depth. Nature 427, 724–727. https://doi.org/10.1038/nature02251.

Mook, W.G., 2001. Environmental isotopes in the hydrological cycle: Principles and applications. IHP-V Technical Documents in Hydrology. vol. No 39. UNESCO.

Mook, W.G., Bommerson, J.C., Staverman, W.H., 1974. Carbon isotope fractionation between dissolved bicarbonate and gaseous carbon dioxide. Earth Planet. Sci. Lett. 22, 169–176. https://doi.org/10.1016/0012-821X(74)90078-8.

Mucci, A., 1983. The solubility of calcite and aragonite in seawater at various salinities, temperatures, and one atmosphere total pressure. Am. J. Sci. 283, 780–799. https://doi.org/10.2475/ajs.283.7.780.

Myrttinen, A., Becker, V., Mayer, B., van Geldern, R., Barth, J.A.C., 2015. Determining in situ pH values of pressurised fluids using stable carbon isotope techniques. Chem. Geol. 391, 1–6. https://doi.org/10.1016/j.chemgeo.2014.10.015.

Nicoli, G., Borghini, A., Ferrero, S., 2022. The carbon budget of crustal reworking during continental collision: clues from nanorocks and fluid inclusions. Chem. Geol. 608, 121025. https://doi.org/10.1016/j.chemgeo.2022.121025.

Ozima, M., Podosek, F.A., 2002. Noble Gas Geochemistry. Cambridge University Press https://doi.org/10.1017/cbo9780511545986.

Pantosti, D., Valensise, G., 1993. Source geometry and long term behavior of the 1980, Irpinia earthquake fault based on field geologic observations. Ann. Geophys. 36. https://doi.org/10.4401/ag-4299.

Parkhurst, D.L., Thorstenson, D.C., Plummer, N., 1980. PHREEQE: A Computer Program for Geochemical Calculations (No. 80–96), Water-Resources Investigations Report. US Geological Survey https://doi.org/10.3133/wri8096.

Patacca, E., Scandone, P., 2007. Constraints on the Interpretation of the CROP-04 Seismic Line Derived from Plio-Pleistocene Foredeep and Thrust-Sheet-Top Deposits (Southern Apennines, Italy). Bollettino Della Societa Geologica Italiana Available to: https://www.ncei.noaa.gov/access/ocean-carbon-acidification-data-system/oceans/Handbook_2007.html Available to:.

Piana Agostinetti, N., Giacomuzzi, G., Chiarabba, C., 2017. Seismic swarms and diffuse fracturing within Triassic evaporites fed by deep degassing along the low-angle alto Tiberina normal fault (central Apennines, Italy). J. Geophys. Res. Solid Earth 122, 308–331. https://doi.org/10.1002/2016JB013295.

Picozzi, M., Bindi, D., Festa, G., Cotton, F., Scala, A., D'Agostino, N., 2022. Spatiotemporal evolution of microseismicity seismic source properties at the Irpinia near-fault observatory, southern Italy. Bull. Seismol. Soc. Am. 112, 226–242. https://doi.org/10.1785/0120210064.

Randazzo, P., Caracausi, A., Aiuppa, A., Cardellini, C., Chiodini, G., D'Alessandro, W., Li Vigni, L., Papic, P., Marinkovic, G., Ionescu, A., 2021. Active degassing of deeply sourced fluids in Central Europe: new evidences from a geochemical study in Serbia. Geochem. Geophys. Geosyst. 22. https://doi.org/10.1029/2021gc010017.

Randazzo, P., Caracausi, A., Aiuppa, A., Cardellini, C., Chiodini, G., Apollaro, C., Paternoster, M., Rosiello, A., Vespasiano, G., 2022. Active degassing of crustal CO_2 in areas of tectonic collision: a case study from the Pollino and Calabria sectors (southern Italy). Front Earth Sci. Chin. 10. https://doi.org/10.3389/feart.2022.946707.

Rizzo, A.L., Caracausi, A., Chavagnac, V., Nomikou, P., Polymenakou, P.N., Mandalakis, M., Kotoulas, G., Magoulas, A., Castillo, A., Lampridou, D., Marusczak, N., Sonke, J.E., 2019. Geochemistry of CO_2-rich gases venting from submarine volcanism: the case of Kolumbo (Hellenic volcanic arc, Greece). Front Earth Sci. Chin. 7. https://doi.org/10.3389/feart.2019.00060.

Sano, Y., Wakita, H., 1985. Geographical distribution of 3He/4He ratios in Japan: implications for arc tectonics and incipient magmatism. J. Geophys. Res. Solid Earth 90, 8729–8741. https://doi.org/10.1029/JB090iB10p08729.

Sano, Y., Wakita, H., Ohsumi, T., Kusakabe, M., 1987. Helium isotope evidence for magmatic gases in Lake Nyos, Cameroon. Geophys. Res. Lett. 14, 1039–1041. https://doi.org/10.1029/GL014i010p01039.

Sano, Y., Takahata, N., Seno, T., 2006. Geographical distribution of $^3He/^4He$ ratios in the Chugoku District, Southwestern Japan. Pure Appl. Geophys. 163, 745–757. https://doi.org/10.1007/s00024-006-0035-0.

Schauble, E.A., Ghosh, P., Eiler, J.M., 2006. Preferential formation of 13C–18O bonds in carbonate minerals, estimated using first-principles lattice dynamics. Geochim. Cosmochim. Acta 70, 2510–2529. https://doi.org/10.1016/j.gca.2006.02.011.

Schön, J.H., 2011. Physical Properties of Rocks: A Workbook. Elsevier Availlable to: https://www.ncei.noaa.gov/access/ocean-carbon-acidification-data-system/oceans/Handbook_2007.html.

Smeraglia, L., Bernasconi, S.M., Berra, F., Billi, A., Boschi, C., Caracausi, A., Carminati, E., Castorina, F., Doglioni, C., Italiano, F., Rizzo, A.L., Uysal, I.T., Zhao, J.-X., 2018. Crustal-scale fluid circulation and co-seismic shallow comb-veining along the longest normal fault of the central Apennines, Italy. Earth Planet. Sci. Lett. 498, 152–168. https://doi.org/10.1016/j.epsl.2018.06.013.

Tamburello, G., Pondrelli, S., Chiodini, G., Rouwet, D., 2018. Global-scale control of extensional tectonics on CO 2 earth degassing. Nat. Commun. 9, 4608. https://doi.org/10.1038/s41467-018-07087-z.

The MathWorks Inc., 2022. MATLAB Version: 9.14.0.2206163 (R2023a). The MathWorks Inc., Natick, Massachusetts, United States.

Ventura Bordenca, C., 2020. Noble Gas Geochemistry in Seismic (Umbria, Italy) and Volcanic (Grand Comore Island, Indian Ocean) Regions: New Methodologies and Implications. Università degli Studi di Palermo.

Venturi, S., Tassi, F., Bicocchi, G., Cabassi, J., Capecchiacci, F., Capasso, G., Vaselli, O., Ricci, A., Grassa, F., 2017. Fractionation processes affecting the stable carbon isotope signature of thermal waters from hydrothermal/volcanic systems: the examples of Campi Flegrei and Vulcano Island (southern Italy). J. Volcanol. Geotherm. Res. 345, 46–57. https://doi.org/10.1016/j.jvolgeores.2017.08.001.

Wiemer, S., 2001. A software package to analyze seismicity: ZMAP. Seismol. Res. Lett. 72, 373–382. https://doi.org/10.1785/gssrl.72.3.373.